Department of Physics and Astronomy
University of Heidelberg

Master Thesis in Physics
submitted by

Sita N. Eberle

from Agios Nikolaos

2013

Photoionization of the beryllium atom

This Master Thesis has been carried out by Sita N. Eberle at the
Max Planck Institute for Nuclear Physics in Heidelberg
under the supervision of PD Dr. José R. Crespo López-Urrutia

Abstract

Photoionisation des Beryllium atoms:

Ziel dieser Arbeit war, eine Quelle für die Erzeugung von Beryllium-Photoionen zu konfigurieren und zu bauen um mit ihnen die sympathetische Laserkühlung hochgeladener Ionen in einer kryogenischen Paulfalle zu ermöglichen. Als atomphysikalischer Mechanismus bietet sich die Zwei-Photonen-Anregung neutraler Beryllium Atome an, bei der der resonante Übergang $1s^2 2s^2\ {}^1S_0 \rightarrow 1s^2 2s2p\ {}^1P_1$ des Atoms bei 235 nm von einer nichtresonanten Transfer des Elektrons ins Kontinuum gefolgt wird. Der apparative Aufbau, die Erzeugung und Anregung des Atomstrahls sowie die Ionenproduktion und Nachweis werden beschrieben. Die experimentellen Ergebnisse betreffen die Untersuchung der Doppler Verbreiterung und der intensitätsabhängigen Sättigung des Übergangs sowohl für die Fluoreszenz- als auch für die Ionenspektren. Schließlich wurden die Wirkungsquerschnitte für den Zwei-Photon-Prozess abgeschätzt. Der Aufbau erfüllt die an ihn gestellten Erwartungen und wird in das Hauptexperiment CryPTEx implementiert.

Photoionization of the beryllium atom:

The task of this thesis was to configure and build a source of beryllium photoions in order to sympathetically cool highly charged ions in a cryogenic Paul trap with them. A suitable process for this purpose is the two-photon ionization of neutral beryllium atoms that is achieved by a resonant excitation of the $1s^2 2s^2\ {}^1S_0 \rightarrow 1s^2 2s2p\ {}^1P_1$ transition at 235 nm of the atom followed by the non-resonant transfer of an electron to the continuum. The instrumental setup, the generation and excitation of the atomic beam and the production and detection of ions are described. The experimental results concern studies of the Doppler broadening and saturation intensity on both fluorescence and ion spectra. Finally the cross sections were estimated for the two photon process. The setup fulfills the required specifications and is being implemented in the main experiment CryPTEx.

Contents

1 Introduction

Very recently observations were made that, if they were proven true, would most likely completely change our understanding of the universe [1], [2]. According to those reports, the fine structure constant α is not constant as believed so far, but varies in space and time. J. Webb, V. Flambaum and their colleagues observed radiation coming from extremely bright quasars that are billions of light years away. While their light travels, it gets partially absorbed by ancient clouds of matter, enabling the determination of the fine structure constant. The result of their observations in the northern sky showed that billions of years ago α used to be about one part in 10^{-5} smaller than today. There are still serious doubts about their results and conclusions. Their further measurements in the southern hemisphere showed a variation of the same order of magnitude in the opposite direction [3]. This would mean that α was this time about 1 part in 10^{-5} larger! The significance of this observation, if confirmed, is huge. It would mean that we have to reconsider the validity of Einsteins general relativity (since one of the basic assumptions requires that the fine structure constant is constant in space and time). At the same time, this could mean good news for a grand unified theory since many of such theories contradict Einsteins equivalence principle. Also "on earth" experiments searching for a variation of α have been performed. The idea behind such experiments is that the Earth as well moves in space and so a minimal variation should be able to be verified in time. For such measurements laser spectroscopy of atomic or ionic transitions is used [5]. With this method, transition frequencies can be measured with a very high accuracy. It is therefore straightforward, that by comparing transitions with a fine structure splitting ΔE_{fs}, a variation in time of α can be measured, since $\Delta E_{\text{fs}} \propto \alpha^2$. A recent atomic clock experiment involving the comparison of Hg^+ and Al^+ clocks over the course of a year [6] suggests an α variation value of $\dot{\alpha}/\alpha = (-1.6 \pm 2.3) \cdot 10^{-17}\,\text{year}^{-1}$ which is consistent with no change. However,

to test the astrophysical claims [8] accuracy still has to be improved by about two orders of magnitude. This means that major improvements of such measurements are needed to settle the question.

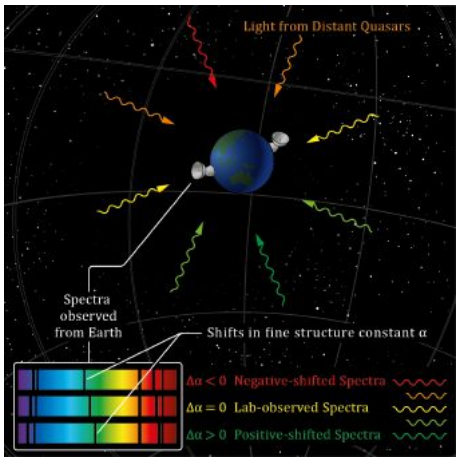

Figure 1.1: Alpha variation as measured by J. Webb, V. Flambaum and their colleagues. Image from Dr. Julian Berengut, UNSW, 2010.

A very promising idea that could provide the desired accuracy, is to use Highly Charged Ions (HCI) to pursue atomic clock experiments. In HCI, α variation effects are increased, since the sensitivity to α increases proportionally to Z_a^2, where Z_a is the effective charge experienced by an outer electron. In order to choose the most suitable transitions and the appropriate HCI, some conditions have to be met. First, the transitions should have a long lifetime (metastable states), such that their frequencies can be measured with high accuracy. Second, one needs lines accessible by laser excitation. Unfortunately, energy differences between levels in HCI are large and increase with Z_a^2, bringing most dipole-allowed transitions beyond the range of lasers. But naturally occuring level crossings and near-degeneracies are found in HCI. When the ion charge is increased, the ordering of orbitals can change, allowing for transitions in the optical regime to appear. Taking all this into account, the two ions with transitions of the highest predicted sensitivity to α variation are Ir^{16+} and Ir^{17+}. At the Max Planck Institute for Nuclear Physics in Heidelberg, an experiment is being set up to achieve a more precise α variation experiment using those advantages of HCI. For this purpose, an electron beam ion trap (EBIT) [9] has been connected to a cryogenic Paul trap [11]. An EBIT [12] is a relatively compact instrument used to produce and trap HCIs. Inside an EBIT, neutral atoms are

ionized by an electron beam that is focused by means of a strong magnetic field, and driven by a high potential difference through the interaction region. The produced ions are confined both by the negative charge of the electron beam and by ring electrodes that control the storage of the ions. Even the highest charge states such as U^{92+} have been produced in an EBIT, making it the perfect instrument for our purpose. However, the HCI trapped in an EBIT have temperatures in the order of hundreds of electronvolts (or $\sim 3 \cdot 10^5\,\mathrm{K}$). Applying evaporative cooling [14] is a first step that cools the ions down to about 28 eV [15] or in the best case even to 12 eV [16]. However, even at such temperatures the Doppler broadening of their lines is huge and its contribution to the transition line widths is forbidding when very high precision is required. This is where the cryogenic Paul trap brings an advantage [11]. The chosen ion, Ir^{17+}, like most HCIs, does not possess transitions appropriate for laser cooling. However, inside a Coulomb crystal prepared in a Paul trap, Ir^{17+} ions could be very effectively cooled down to the millikelvin range by means of sympathetic cooling. Such an experiment was successfully carried out in a Penning trap [18]. We choose a Paul trap since it offers higher accuracy for this type of experiments and allows better optical access. The Paul trap that will be used, was built and commissioned at the Max Planck Institute for Nuclear Physics in collaboration with the Ion Trap Group at the University of Århus. The ion that will be used to sympathetically cool down Ir^{17+} ions is the singly charged beryllium ion Be^+. Be^+ has a charge-to-mass ratio close to that of Ir^{17+}, a fact that allows more effective cooling. The closed-cycle cooling transition will be the $2s^2\,S_{1/2} \leftrightarrow 2p^2\,P_{3/2}$ transition at a wavelength of 313 nm [20]. A laser with the required output wavelength is already in operation and provides a high power of about 700 mW, more than sufficient to achieve the envisioned cooling effect. In this context, one of the most important remaining requirements was the production of Be^+ ions, a task that was accomplished during this master thesis.

The task of photoionizing beryllium turned out to be a technical challenge. First, a stable atomic beam of a metal with a melting temperature of 1560 K needed to be attained. Second, handling a toxic metal like beryllium requires great attention and planning of all necessary measures that have to be taken. Once all preparations were made and the first photoionization signals were detected, a number of interesting effects were brought to light. The measurements presented in this thesis involve studies of the Doppler effect of the spectral signals, studies of the saturation

broadening of the spectra as a function of the laser beam intensity and, finally, the determination of the expected two-photon ionization cross section of beryllium, an important measure as we want to have high-efficiency loading of the Paul trap in order to minimize Be contamination as well as the gas load.

Chapter 2 of this thesis deals with the relevant theoretical basic knowledge. Chapter 3 deals with the experimental setup that was constructed during this thesis and with the setup of the laser used for photoionization. Chapter 4 presents the experimental results on Doppler broadening effects, saturation broadening and an experimental estimation of the two photon ionization cross section of beryllium. Finally, Chapter 5 presents a summary of the thesis and an outlook.

2 Theory

2.1 Photoionization

Photoionization is the process in which a photon of sufficient energy reacts with an atom or ion of charge q (Z^q) and releases an electron, resulting in a higher ionization state of the atom or ion (Z^{q+1}). During this process the photon is absorbed and transfers its energy to an electron which turns into a free electron afterwards according to:

$$\hbar\omega + Z^q \rightarrow Z^{q+1} + e^-. \tag{2.1}$$

In order to ionize an atom, the energy of the photon has to be greater than the ionization potential E_{IP} of the specific atom. If this threshold is not reached, only resonant interatomic transitions may occur. Resonant transitions are called so, because, unlike photoionization, the photon energy absorbed by an electron has to equal the exact value energy difference between levels. If the energy difference between initial state i and final state f is ΔE_{if}, the incoming photon has to have the exact energy $\hbar\omega = \Delta E_{if}$. In the case of photoionization, the energy equilibrium can be described by following equation:

$$\hbar\omega = E_{\mathrm{PI}} + \frac{k^2}{2}, \tag{2.2}$$

where $\frac{k^2}{2} = E_{\mathrm{kin}}$ stands for the kinetic energy of the free electron described classically (k is the wavenumber). In the case of a photon energy higher than the ionization potential, the remaining energy can take the form of a photon of longer wavelength. This inelastic process is known as Compton scattering.

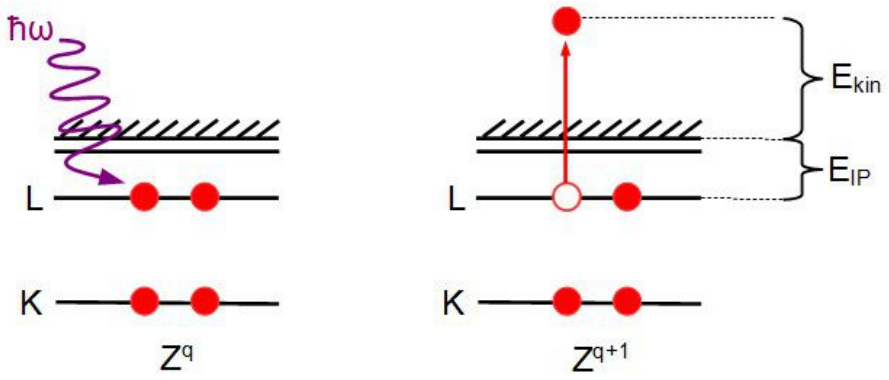

Figure 2.1: Scheme of a one-photon ionization process. A photon of energy $\hbar\omega$ that corresponds to at least the ionization potential of an atom sets one electron free. The difference of the initial energy of the photon $\hbar\omega$ and the potential energy of the electron E_{IP} equals the final kinetic energy of the free electron. $E_{\mathrm{kin}} = \hbar\omega - E_{\mathrm{IP}}$.

2.1.1 Multiphoton processes in atoms

The ionization of an atom (or other quantum system) is called a multi-photon (MPI) or nonlinear ionization when the condition $E_{\mathrm{ph}} < E_{\mathrm{ion}}$ is fulfilled, where E_{ph} is the photon energy of radiation and E_{ion} is the binding energy or the outermost electron. In order to attain ionization in this case, more than one photon is required, so that $n \cdot E_{ph} > E_{ion}$, where n stands for an integer number of photons. In the case of non-resonant multiphoton ionization (NR-MPI), Bohrs postulate according to which a transition in an atom occurs when one photon with an energy that corresponds to the exact energy difference between the two atomic levels, is clearly violated. The probability for such a process to occur results from the quantum mechanical uncertainty principle of energy and time according to which: $\Delta E \cdot \Delta t \geq \frac{\hbar}{2}$. This means that for a small time interval Δt, the energy defect ΔE can be large. Such transitions and states are called virtual and have extremely short lifetimes compared to real transitions and states. Thus, a MPI process can occur by means of virtual intermediate transitions of an electron from its initial state to the continuum. This process is however very complex. Keldysh [19] was the first to study the case in which the number of photons is $n \gg 1$ and the electric field strength F is much smaller than the atomic field strength F_a, i.e. $F \ll F_a$. The character of this

process is determined by the Keldysh adiabatic parameter [42]

$$\gamma = \frac{\omega\sqrt{2|E_{\text{ion}}|}}{F}. \tag{2.3}$$

As can be assumed from equation 2.3, the process depends basically on three parameters: the frequency ω, the electric field strength F, and the binding energy of the atom E_{ion}. In the case of $\gamma^2 \gg 1$, the MPI probability w is determined by the lowest order perturbation theory formula:

$$w = \sigma_n(\omega, \rho)\left(\frac{cF^2}{8\pi\hbar\omega}\right)^n = \sigma_n(\omega, \rho)\left(\frac{I}{\hbar\omega}\right)^n, \tag{2.4}$$

where $I = cF^2/8\pi$ is the intensity amplitude, F is the field strength, ρ is the radiation ellipticity, and $\sigma_n(\omega, \rho)$ is the generalized MPI cross section. For the case of one photon ($n = 1$), formula 2.4 becomes the well known formula for the rate of one-photon ionization. Now in the case of $\gamma^2 \ll 1$, nonlinear ionization is tunneling in an alternating field. In this case, the rate of nonlinear ionization depends on the field strength F exponentially:

$$w = \exp\left[-2(2E_{ion})^{3/2}/3F\right]. \tag{2.5}$$

The actual difference between multiphoton and tunneling ionization processes lies essentially in the frequency dependence of their rates. According to equations 2.4 and 2.5, the dependence is zero for tunneling ionization significant for MPI. Apart from that, tunneling ionization is typically realized with lasers operating in the infrared regime, while in the visible, UV and VUV regions MPI is more common. In very strong fields, above threshold ionization (ATI) can occur, a multi-photon process in which an atom is ionized by more than the required number of photons [31]. Such processes have been investigated in detail with visible and infrared laser sources. The ultraviolet (UV) and X-ray spectral range have been less intensively studied, since intense lasers with such short wavelengths have been a challenge during the past few decades. In the next Section the special case of resonant enhanced photoionization is treated.

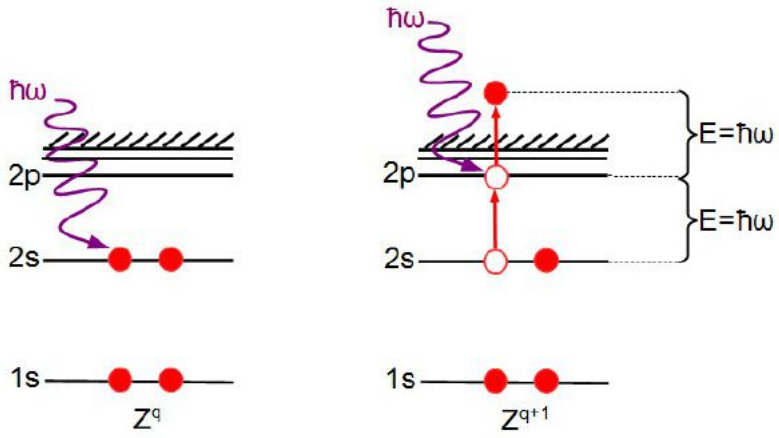

Figure 2.2: Two-photon photoionization process

2.1.2 Resonance enhanced ionization process

Resonance enhanced photoionization is a special case of MPI in which at the first step the energy of m photons is equal to the transition energy between an initial state i and an excited state k, i.e. $m\hbar\omega = E_{ik}$. In order to reach ionization from the excited level k another integer number of $n - m$ photons is required adding up to the total number of photons required for ionization n. See figure 2.2 for the case of a process with m=1 and n=2. In the case of resonance enhanced MPI formulae 2.4 and 2.5 cannot be applied. The ionization rate for such processes is much higher than the rate of non-resonant multiphoton ionization. If spontaneous emission is the dominating process that takes place, resonance enhanced ionization is a cascade process and the probability of ionization w_{iE} can be obtained by simply multiplying the excitation probability W_{ik} with the ionization rate $\omega_i E$ of the resonance state k:

$$w_{iE} = W_{ik} w_{kE}. \tag{2.6}$$

In weak fields, the rate of resonance-enhanced ionization can be given by following

formula [42]

$$W = W_{ki} w_{Ek} = \frac{|V_{ki}^{(m)}|^2}{(E_k - E_i - m\hbar\omega)^2 + \gamma_k^2/4} w_{Ek} = \tag{2.7}$$

$$|z_{ik}^{(m)} F^m|^2 \frac{\Gamma_k(F)}{(E_k - E_i - m\hbar\omega)^2 + \gamma_k^2/4}, \tag{2.8}$$

where

$$V_{ki}^{(m)} = z_{ki}^{(m)} F^m \tag{2.9}$$

is the compound matrix element of m-photon excitation of the resonance level k, $w_{Ek} = \Gamma_k(F)$ is the ionization width of level k, z_{ki} is the transition dipole moment, F is the field strength and γ_k is the natural line width of the level k.

2.1.3 Theoretical determination of the resonant two photon ionization cross section of beryllium

Formula 2.7 can be used to roughly approach the resonance enhanced multiphoton ionization cross section of beryllium. Firstly the equation is rewritten for a cross section instead of a rate and for an ionization process involving a one photon excitation process first (m=1). Here the $(E_k - E_i - m\hbar\omega)^2$ term in the denominator has been set to zero since we consider the case where the laser frequency corresponds exactly the required transition frequency:

$$\sigma_{tot} = \frac{\left|z_{ik}^{(1)}\right|^2 \cdot \frac{2\hbar\omega}{\epsilon_0 c}}{\gamma_k^2/4} \cdot \sigma_{Ek} = \frac{\left|z_{ik}^{(1)}\right|^2 \cdot \frac{2\hbar\omega}{\epsilon_0 c}}{\hbar^2/4\tau_k^2} \cdot \sigma_{Ek} = \frac{8\left|z_{ik}^{(1)}\right|^2 \omega \cdot \tau_k^2}{\hbar\epsilon_0 c} \cdot \sigma_{Ek} \tag{2.10}$$

Here σ_{Ek} stands for the ionization cross section of the excited $^1P_1$ state of Be taken from [35] to be $\sigma_{Ek} = 20\,\mathrm{Mb} = 2 \cdot 10^{-21}\,\mathrm{m}^2$. $z_{ik}^{(1)}$ is the dipole matrix element of the excitation to the excited level k. The well known relation of a transition dipole matrix is [37]

$$z_{ik} = e \int \psi_i^* \mathbf{r} \psi_k d\tau \tag{2.11}$$

with $d\tau$ expressing an integration over all three space coordinates of the electron. In order to get to the value of the transition matrix element, we use the relation with the Einstein coefficient of spontaneous emission according to which [37]

$$A_{ik} = \frac{2}{3}\frac{e^2\omega_{ik}^3}{\epsilon_0 c^3 \cdot h} \cdot \left| \int \psi_i^* \mathbf{r} \psi_k d\tau \right|^2 \tag{2.12}$$

so $\left|z_{ik}^{(1)}\right|^2$ can be expressed according to equation 2.12 as

$$\left|z_{ik}^{(1)}\right|^2 = \frac{3}{2}\frac{\epsilon_0 c^3 h}{\omega_{ik}^3} \cdot A_{ik}. \tag{2.13}$$

A_{ik} and τ_k can be found in various publications, for instance according to [36] $A_{ik} = 5.54 \cdot 10^8\,\mathrm{s}^{-1}$ and $\tau_k = 1.786 \cdot 10^{-9}\,\mathrm{s}$. Inserting these values into 2.10 gives us the value $\sigma_{tot} = 1.467 \cdot 10^{-41}\,\mathrm{m}^4{\cdot}\mathrm{s}$.

2.2 Oscillator strength and absorption cross section

Transition probabilities in atoms or molecules can be expressed through their oscillator strength f, which is an experimentally determinable quantity. In order to understand what the oscillator strength really is, we imagine a valence electron in a state i that behaves like a classical oscillator with an oscillating charge $q = -e$. By absorbing a photon, the electron can reach a number of energetically higher states E_k undergoing the transition $E_i \rightarrow E_k$. For every such allowed transition the oscillator strength $f_{ik} < 1$ corresponds to only a part of the total oscillator strength. When knowing the oscillator strength of a specific excitation, the absorption cross section for this transition can be easily calculated by:

$$a_{ik} = \frac{4\pi e^2 f_{ik}}{m_e c}. \tag{2.14}$$

Also, the three Einstein coefficients for absorption, stimulated emission and spontaneous emission can be easily determined. Here we are interested in the coefficient

for absorption which is equal to:

$$B_{ik} = \frac{4\pi^2 e^2 f_{ik}}{m_e h\nu c}. \tag{2.15}$$

For the purpose of this thesis, neutral beryllium atoms were ionized by a two photon process. The first step of this process is the excitation of the atom from the ground state $2s^2\ {}^1S$ to the excited state $2s2p\ {}^1P$. According to calculations made by G. Tachiev and F. Fischer [23], the oscillator strength of this transition is 1.3726(21). Other calculations move in the same range and experimental results show similar results between 1.339 [28] and 1.40(6) [30]. The cross section of this process is also easily calculated when the absorption coefficient is known [29], according to

$$\sigma(\omega) = \frac{\hbar\omega B_{ik} g(\omega)}{c}, \tag{2.16}$$

or with the assumption of a delta peak,

$$\sigma_0 = \frac{\hbar\omega_{ik} B_{ik}}{c}. \tag{2.17}$$

Finally, in terms of the coefficient $\mathrm{A_{ik}}$, the absorption cross section is

$$\sigma(\omega) = \frac{g_k}{4g_i}\lambda_{ki}^2 g(\omega) A_{ki}, \tag{2.18}$$

or again with a sharp peak at $\omega_i k$

$$\sigma_0 = \frac{g_k}{4g_i}\lambda_{ik}^2 A_{ki}. \tag{2.19}$$

2.3 Decay rates and transition strengths in real atoms

Real atoms have a large number of energy levels so many decay transitions are possible. When an atom is in an upper energy level E_j, it will relax to a number of different lower levels E_i via both radiative and non-radiative decay mechanisms.

The total decay rate is then given by the sum over all decay possibilities:

$$\gamma_j = \frac{1}{\tau_j} = \sum_{E_i<E_j} \gamma_{ji} = \sum_{E_i<E_j} \left[\gamma_{\mathrm{rad,ji}} + \gamma_{\mathrm{nr,ji}}\right] \tag{2.20}$$

The radiative lifetime τ_j of an upper energy level can be measured by observing the fluorescent light emission from the upper level E_j to a lower lying level E_i. The intensity of the fluorescence light will then be proportional to $\gamma_{\mathrm{rad,ji}}$ and to the upper level population N as a function of time:

$$I_{\mathrm{fl}} = \mathrm{const} \times \gamma_{\mathrm{rad,ji}} N_{\mathrm{j}}(t) \tag{2.21}$$

Taking the total decay rate for all transitions, $N_j(t)$ decays exponentially according to:

$$I_{fl} = \mathrm{const} \times N_j(t) = \mathrm{const} \times \exp\left[\frac{-t}{\tau_j}\right]. \tag{2.22}$$

The radiative part of the total decay has an analogy to the radiative decay of a classical oscillator. An oscillating atom is like a classical dipole when it comes to radiating photons at discrete oscillation frequencies and decay with time. The classical electron oscillator (CEO) radiative decay rate is given by

$$\gamma_{\mathrm{rad,ceo}} = \frac{e^2\omega_a^2}{6\pi\epsilon mc^3} \approx 2.47 \cdot 10^{-22} \times n{f_a}^2, \tag{2.23}$$

where n is the refractive index of the medium, and f_a is the oscillation frequency in Hz. A rule of thumb is that the radiative lifetime of a classical CEO in ns is

$$\tau_{\mathrm{rad,ceo}} \approx \frac{45\left(\lambda_0\left[\mu m\right]\right)^2}{n} \tag{2.24}$$

for example at an ultraviolet (UV) wavelength of $0.235\,\mu$m, the classical oscillator lifetime is $\tau_{\mathrm{rad,ceo}} \approx 2.49\,$ns. In general the rule is that the radiative decay rate for a real atomic transition is always smaller than or equal to the radiative decay rate for the CEO at the same frequency, i.e. $\tau_{\mathrm{rad,ji}} \geq \tau_{\mathrm{rad,ceo}}$. The strength of the response of a real atomic transition relative to the response of a CEO at the same frequency

is called oscillator strength and can be written as:

$$F_{\mathrm{ji}} = \frac{\gamma_{\mathrm{rad,ji}}}{3\gamma_{\mathrm{rad,ceo}}} = \frac{\tau_{\mathrm{rad,ceo}}}{\tau_{\mathrm{rad,ji}}}. \tag{2.25}$$

The factor 3 has to do with polarization properties of real atoms compared to classical oscillators.

2.4 The beryllium atom and singly charged ion

Beryllium belongs to the second group of the periodic table (see figure 2.3 below), the group of alkaline earths. Its atomic number is $Z = 4$ and its electronic configuration in the ground state is $1s^2 2s^2$. As a free element it is steel-gray, strong, lightweight and brittle. Beryllium is as well a very toxic metal and especially causes damage when inhaled. It is corrosive to tissue, and can cause berylliosis, a chronic

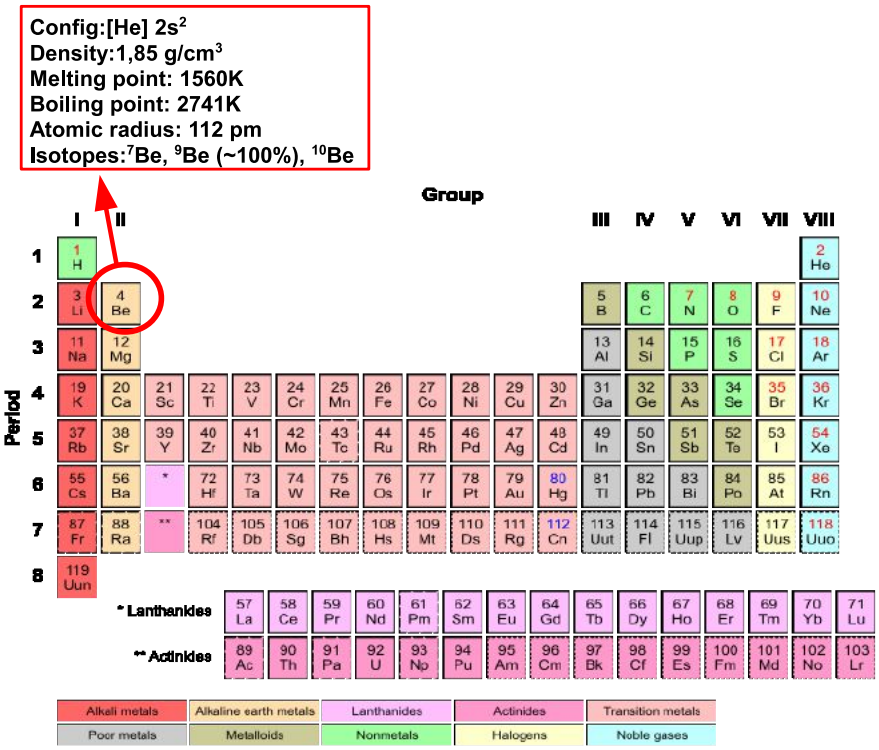

Figure 2.3: Beryllium in periodic table

life-threatening allergic disease. Beryllium at room temperature has a close-packed hexagonal crystal structure. Other physical properties are shown on figure 2.3. The

λ_{vac}[nm]	234.9329
$A_{ki}[s^{-1}]$	$5.54 \cdot 10^8$
f_{ik}	1.38
S_{ik}	10.6
$log(g_i f_{ik})$	0.139

Table 2.1: Properties of the transition $1s^2 2s^2\ ^1S_0$-$1s^2 2s2p\ ^1P_1$, marked in green on diagram 2.4. Data taken from [13].

melting point of beryllium lies at 1560 K, a reasonably high value so there is negligible vapor pressure at room temperature. Additionally, beryllium is a mono-isotopic element, which means it has only one stable isotope, ^{9}Be, with a nuclear spin of $-3/2$. All other isotopes of beryllium are extremely rare and unstable. ^{10}Be has the longest lifetime ($1.36 \cdot 10^6$ years) followed by ^{7}Be which has a lifetime of 53.12 days. ^{6}Be, ^{8}Be, ^{11}Be, ^{13}Be and ^{14}Be all have extremely short lifetimes (shorter than 10^{-16} s). Furthermore beryllium has very high ionization potentials and strong polarization while bonded to other kinds of atoms.

Spectroscopic properties

On figure 2.4, a Grotrian diagram of the neutral beryllium atom is presented showing all energetic levels up to the $1s^2 2s3p\ ^1P_1$ level. It is apparent that some levels have a fine structure, denoted correspondingly. All (dominating) E1 transitions are marked in the diagram with arrows. The green arrows corresponds to the most important transitions for this thesis. From now on, whenever mentioning Be or Be^+, the stable isotope ^{9}Be is implied. As mentioned before, ^{9}Be has a nuclear spin of $-3/2$. Therefore, the element has hyperfine structure levels that are not shown on the diagram since they are beyond the scope of this thesis. The most interesting transition for this thesis is the $1s^2 2s^2\ ^1S_0$-$1s^2 2s2p\ ^1P_1$ transition. Table 2.1 shows the most important characteristics of this transition.

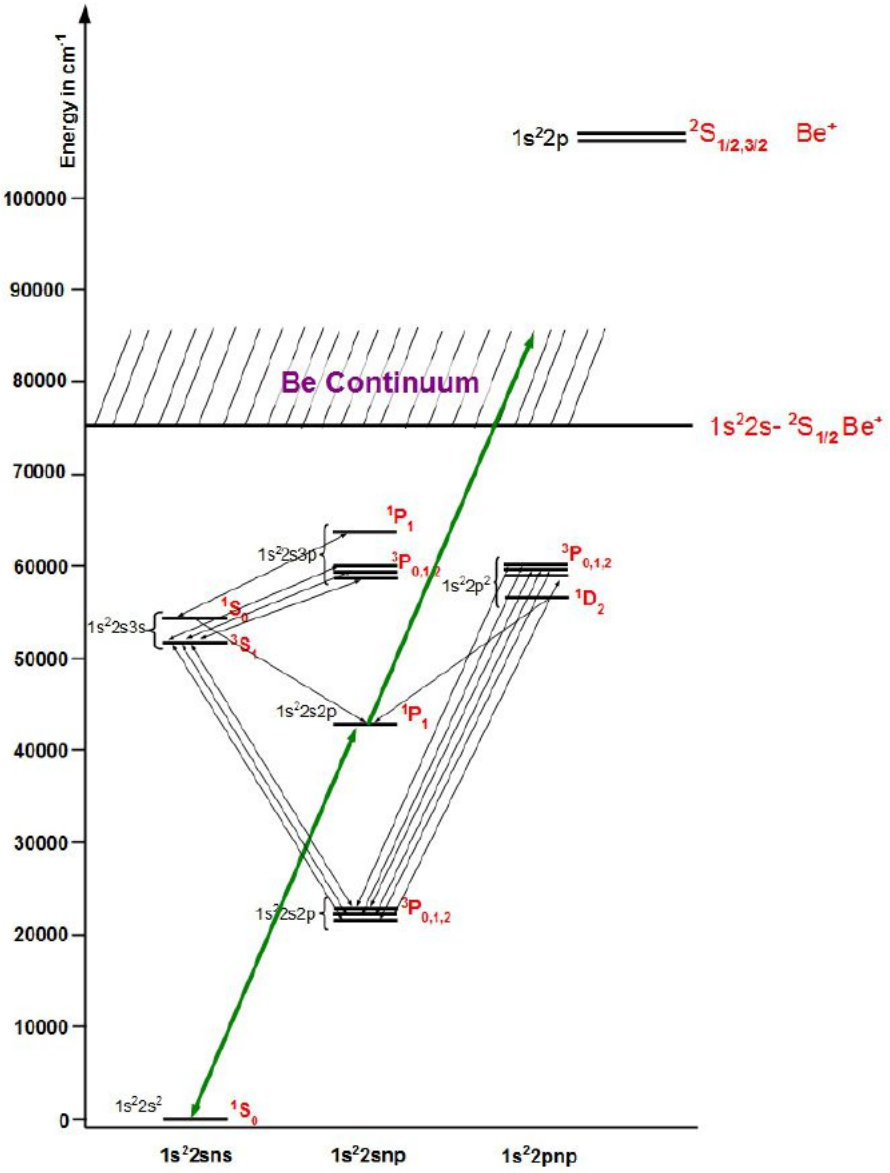

Figure 2.4: Grotrian diagram of Be transitions until an energy of about 65000 cm^{-1} and main levels of the Be^+ ion [7]. Levels and distances are to scale except of the fine structure triplets. Here distance has been exaggerated in order to distinguish fine structure levels.

2.5 Non-linear optics

For the generation of UV radiation we utilize the process of second harmonic generation (SHG). This is a non-linear effectand therefore the fundamentals of non-linear optics are discussed. Non-linear optics is the branch of optics that studies the in-

teraction of electromagnetic radiation with matter in which the matter responds nonlinearly to the incident radiation fields. Typically this nonlinearity can only be observed at very high intensities, which is why it was not observed until the invention of lasers. The first nonlinear optics experiment of the laser era was performed in 1961 by Peter Franken and co-workers at the university of Michigan [22], who managed to create a detectable second harmonic generation signal. In the following Section, the aspects of nonlinear optics related to second harmonic generation will be handled.

2.5.1 Theory of non-linear optics

In linear optics, propagation of light is independent of the field intensity. The dependence of the polarization on the electric field strength is linear and one writes:

$$\mathbf{P} = \epsilon_0 \chi \mathbf{E}, \tag{2.26}$$

where χ is the linear susceptibility and ϵ_0 the dielectric constant. So for $\mathbf{E} = A\cos\omega t$, we get

$$\mathbf{P} = \epsilon_0 \chi A \cos\omega t. \tag{2.27}$$

It also follows that the electric displacement is

$$\mathbf{D} = \epsilon_0 \mathbf{E} + \mathbf{P} = \epsilon_0 (1+\chi)\mathbf{E} = \epsilon_0 \epsilon \mathbf{E}. \tag{2.28}$$

where $\epsilon = 1 + \chi$ is the relative dielectric constant. This linear approximation is only good for small polarization shifts and not too high field intensities. In nonlinear optics, however, the response of materials to an electrical field is non-linear. Here higher orders in the expansion of χ have to be taken into account:

$$\chi(\mathbf{E}) = \chi^{(1)} + \chi^{(2)}\mathbf{E} + \chi^{(3)}(\mathbf{E}\cdot\mathbf{E}). \tag{2.29}$$

Thus, the polarization becomes

$$\mathbf{P} = \epsilon_0 \big(\chi^{(1)}\mathbf{E} + \chi^{(2)}(\mathbf{E}\cdot\mathbf{E}) + \chi^{(3)}(\mathbf{E}\cdot\mathbf{E})\cdot\mathbf{E}\big). \tag{2.30}$$

Here $\chi^{(i)}$ stands for the dielectric susceptibility of order i. Until now χ was treated as a scalar. Such a treatment is sufficient for isotropic media, but for anisotropic (non-linear) media and fields of high intensity, $\chi^{(i)}$ shows tensor characteristics.

2.5.2 Sum Frequency Generation and the special case of Second Harmonic Generation

Nonlinear effects, are not only fascinating in itself but are also very useful for scientific applications. Laser frequencies that could not be obtained until a couple of years ago, now can be easily produced by means of Sum Frequency Generation (SFG) and its special case of Second Harmonic Generation (SHG). Sum frequency is obtained by overlapping two monochromatic fields $\mathbf{E}_1$ and $\mathbf{E}_2$ in a non-linear medium. Due to the total field strength $\mathbf{E}(\mathbf{r},t)$ and non-linear polarization $\mathbf{P}^{(2)}(\mathbf{r},t)$, mixed frequencies arise. $\mathbf{E}(\mathbf{r},t)$ can be written as:

$$\mathbf{E}(\mathbf{r},t) = \mathbf{E}_1(\mathbf{r},t) + \mathbf{E}_2(\mathbf{r},t) = \frac{1}{2}\left[\mathbf{E}'(\mathbf{r},\omega_1)e^{i\omega_1 t} + \mathbf{E}'(\mathbf{r},\omega_2)e^{i\omega_2 t} + c.c\right] \tag{2.31}$$

where $\mathbf{E}'(\mathbf{r},\omega_i)$ with $i = 1.2$ stands for position and frequency dependent amplitudes, ω_i stand for the frequencies of the two laser beams, $\mathbf{r}$ stands for the space coordinates and c.c is an abbreviation for complex conjugate.

$$\begin{aligned}
\mathbf{P}^{(2)}(\mathbf{r},t) =& \frac{1}{2}\left[\mathbf{P}'(\mathbf{r},2\omega_1)e^{i2\omega_1 t}\right] \\
&+\frac{1}{2}\left[\mathbf{P}'(\mathbf{r},2\omega_2)e^{i2\omega_2 t}\right] \\
&+\frac{1}{2}\left[\mathbf{P}'(\mathbf{r},\omega_1+\omega_2)e^{i(\omega_1+\omega_2)t}\right] \\
&+\frac{1}{2}\left[\mathbf{P}'(\mathbf{r},\omega_1-\omega_2)e^{i(\omega_1-\omega_2 t)}\right] \\
&+\frac{1}{2}\left[\mathbf{P}'(\mathbf{r},0)\right]
\end{aligned} \tag{2.32}$$

with the amplitude $\mathbf{P}'(\mathbf{r},\omega_i+\omega_j) = \epsilon_0\chi^{(2)}\mathbf{E}'(\mathbf{r},\omega_i)\cdot\mathbf{E}'(\mathbf{r},\omega_j)$. It is obvious from equation (2.32) that the non-linear polarization $\mathbf{P}^{(2)}(\mathbf{r},t)$ has components with frequencies $2\omega_1$, $2\omega_2$, $\omega_1+\omega_2$, $\omega_1-\omega_2$ and a constant component. Now in the special case of SHG, the two frequencies ω_1 and ω_2 have the same value $\omega_1 = \omega_2 = \omega$, so

$\mathbf{P}^{(2)}(\mathbf{r},t)$ becomes:

$$\mathbf{P}^{(2\omega)}(\mathbf{r},t) = \frac{1}{2}\epsilon_0\chi^{(2)}\mathbf{E}'(\mathbf{r},\omega)^2 \cdot e^{2i\omega t}, \tag{2.33}$$

or with $\mathbf{E}'(\mathbf{r},\omega_i) = \mathbf{E}'(\omega_i) \cdot e^{-i\mathbf{k}_i\mathbf{r}}$,

$$\mathbf{P}^{(2)}(\mathbf{r},t)_{2\omega} = \frac{1}{2}\left[\epsilon_0\chi^{(2)}\mathbf{E}'(\omega)^2 \cdot e^{-i[2\mathbf{kr}-2\omega t]}\right], \tag{2.34}$$

where $\mathbf{k}_i = \frac{2\pi}{\lambda_i}\mathbf{e}_{\mathbf{k}_i}$ stands for the wave vector. This means that the output power of the second order polarization $\mathbf{P}^{(2)}(\mathbf{r},t)_{2\omega}$ is a wave with frequency 2ω and wave vector $2\mathbf{k}$.

2.5.3 Methods of phase matching

For the SHG wave to be emitted, the original fundamental wave and the generated wave of double frequency have to propagate synchronously in phase to allow for efficient conversion of ω to 2ω:

$$n_\omega = n_{2\omega}. \tag{2.35}$$

This condition is called phase matching. If this condition is not met, conversion in the medium will still take place, but a large part of the emitted radiation at different positions will be eliminated through destructive interference or it is reconverted to the fundamental wave. The phase matching condition cannot be met in isotropic materials. Therefore normally birefringent materials are used. For such materials, refracted light splits into an ordinary ray with an isotropic refractive index and an extraordinary ray with an anisotropic refractive index. The anisotropic refractive index is dependent on the angle of incidence. The phase matching condition can be met by using an appropriate crystal. Some examples of crystals used as non-linear optic material are crystals such as KTB, BBO, $LiNbO_3$ LBO, periodically poled polymers or liquid crystals.

Critical phase matching

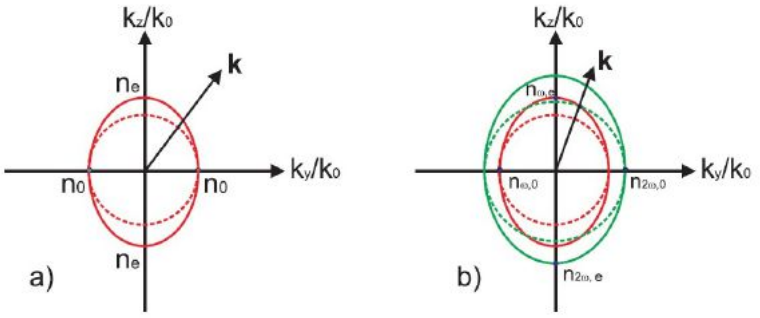

Figure 2.5: Refraction index ellipsoid. (a) For the fundamental wave. The red solid line shows the refraction index dependence of the extraordinary ray while the dashed line shows the dependence of the ordinary ray. (b) The solid and dashed green lines show the dependence of the extraordinary and ordinary waves of the harmonic wave. Red is same as in (a) and for the intersection points $n_{2\omega,e}(\theta) = n_{\omega,o}$ is fulfilled. Taken from [27].

In critical phase matching (CPM) the interacting beams are aligned at some angle to the axes of the refraction index ellipsoid. The refraction index ellipsoids for fundamental and harmonic waves are different but two intersection points exist. When the polarization of the fundamental wave is chosen to propagate as an ordinary wave in the crystal and the harmonic as an extraordinary wave, the phase matching is called type I phase matching and if reversed type II phase matching. In both cases an angle θ needs to exists for which the condition $n_{2\omega,e}(\theta) = n_{\omega,o}$ is fulfilled.

Noncritical phase matching

Noncritical phase matching (also called 90° phase matching) uses the fact that the extraordinary wave and the ordinary wave can have different Poynting vectors in birefringent materials. For this reason the interaction length between fundamental and harmonic wave can become shorter, leading to a lower conversion efficiency (walk-off). However, when the incoming angle of the fundamental wave with respect to the optical axis of the crystal is 90°, the Poynting vectors can be made to coincide. Furthermore, the phase mismatch is minimized by adjusting the crystal temperature such that the phase velocities of the interacting beams are equal.

Quasi phase matching

For quasi phase matching (QPM), instead of a homogeneous nonlinear crystal, a material with spatially modulated nonlinear properties is used. The basic idea is to allow for a phase mismatch for some distance but to reverse the nonlinear interaction at positions where the conversion direction would be at opposite phase. In

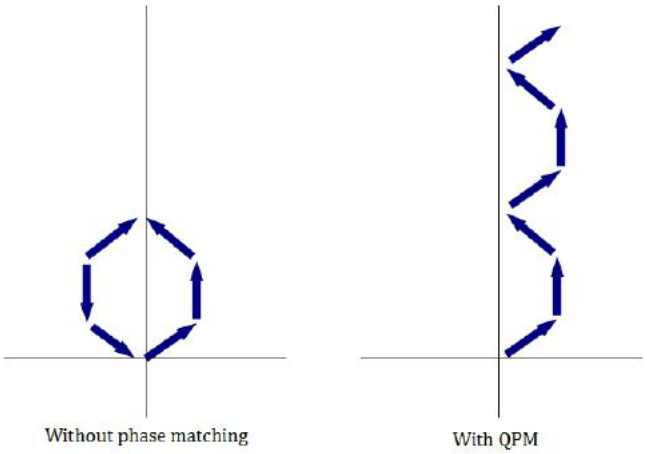

Figure 2.6: Explanation of QPM, modified from [43].

figure 2.6 the principle of QPM is illustrated. The blue arrows represent the complex amplitude contributions of different parts of the crystal to the harmonic wave. If there is no phase matching, the contributions cannot add up constructively over a long distance. When using QPM however, the sign of the contributions is reversed at the point where they would otherwise interfere destructively. This method is only slightly less efficient than real phase matching. However, QPM allows to use the same polarization direction for all waves, leading to much higher conversion efficiencies than real phase matching because of possible higher non-linear coefficients. Additionally this method shows no walk-off.

2.5.4 Frequency doubling of a Gaussian beam and conversion efficiency

One solution of the Helmholtz equation are Gaussian rays, with a field distribution given by

$$E(x,y,z) = \frac{E_0}{1+ir} e^{ikz-i\omega t} e^{\frac{(x^2+y^2)}{\omega_0^2(1+ir)}}. \tag{2.36}$$

Here ω_0 is the beam waist, b is the confocal parameter $b = \omega_0^2 k$ and $r = \frac{2z}{b}$. The figure below represents a Gaussian ray passing through a crystal. The minimum beam waist ω_0 of the Gaussian ray is reached at the focus point f, so $z = f$ (see figure 2.7. In this figure δ_0 is half the diffraction angle and ρ describes the angle between the fundamental wave and the second harmonic wave after passing through the crystal.

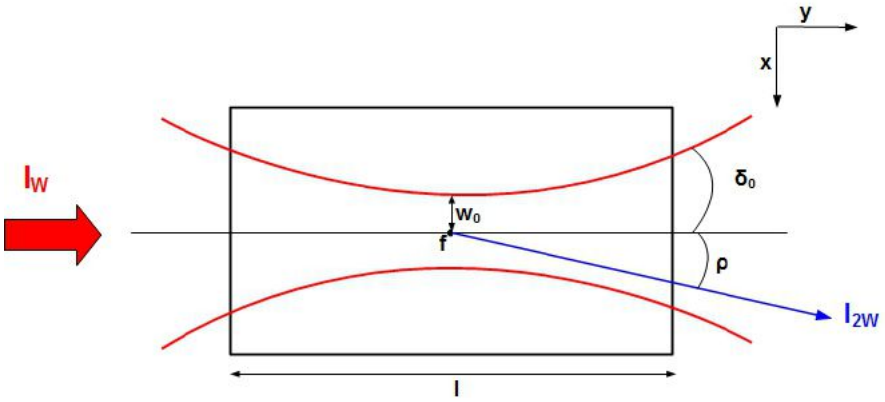

Figure 2.7: Gaus ray parameters in a crystal of length l. I_w and I_{2w} are the fundamental and harmonic intensities.

For the electric field of the fundamental wave the following equation takes effect with the coordinates (x', y', z').

$$E_1(x',y',z') = E_0 \left[\frac{1}{(1+ir')}\right] e^{ik_1 z'} e^{-\frac{(x'^2+y'^2)}{\omega_0^2(1+ir')}} e^{-\frac{1}{2}\alpha_1 z'}. \tag{2.37}$$

Here α_1 is the absorption coefficient of the fundamental wave, $r' = \frac{2(z'-f)}{b}$ and $b = \omega_0^2 k_1$ is the confocal parameter. The nonlinear polarization is proportional to the modulus of the electric field amplitude squared. In the far field, contributions of

all infinitesimal crystal slices to the harmonic wave are added up. For the outgoing power we then have [25]:

$$P_2 = \frac{16\pi^2(\chi^{(2)})^2 l P_1^2}{\lambda_1^3 n_2 n_1 \epsilon_0 c} e^{-\alpha' l + \mu\alpha l} \cdot h(\sigma, B, \xi, \mu, \kappa), \tag{2.38}$$

where P_1 stands for the incoming and P_2 for the outgoing power. n_1 and n_2 stand for the refractive indexes of air and the crystal respectively. μ has to do with the position of the waist,λ_1 is the fundamental wavelength and $\chi^{(2)}$ is the nonlinearity of the crystal. $h(\sigma, B, \xi, \mu, \kappa)$ is the Boyd-Kleinman factor [26] defined as

$$h(\sigma, B, \xi, \mu, \kappa) = e^{\mu\alpha l} \int_{-\xi(1-\mu)}^{\xi(1+\mu)} dr dr' \frac{e^{-\kappa(r'+r)+i\sigma(r'-r)-\beta^2(r'-r)^2}}{(1+ir)(1-ir')}, \tag{2.39}$$

with the parameters $\sigma = \frac{1}{2}b\Delta k$, $\xi = \frac{l}{b}$, $B = \frac{\rho\sqrt{lk_1}}{2}$, $\alpha' = \alpha_1 + \frac{\alpha_2}{2}$, $\kappa = \frac{1}{2}(\alpha_1 - \frac{\alpha_2}{2})b$ and $\mu = \frac{(l-2f)}{l}$.
Parameter B is proportional to the birefringence angle ρ, since $\sqrt{lk_1}$ is constant. B stands for how much the fundamental and harmonic wave move away from each other or, in other words the walk-off of the two waves and ξ has to do with the waist of the beam (focusing parameter). σ is a unit of the phase mismatch Δk. Finally the losses of power through absorption of the fundamental and harmonic waves are parametrized by κ, while α_2 corresponds to the absorption coefficient of the harmonic wave in the crystal. Optimizing the Boyd-Kleinman factor which means choosing the best combination of the parameters σ, B, ξ, σ and μ, maximizes the outgoing power P_2. According to Kleinman and Miller [24] the optimal focus position for negligible absorption ($\kappa = 0$) is in the center of the crystal ($\mu = 0$) and so the outgoing power becomes:

$$P_2(0) = \frac{16\pi^2(\chi^{(2)})^2 l P_1^2}{\lambda_1^3 n_2 n_1 \epsilon_0 c} e^{-\alpha' l} \cdot h(\sigma, B, \xi) \tag{2.40}$$

with

$$h(\sigma, B, \xi) = \frac{1}{4\xi} \int_{-\xi}^{\xi} \int_{-\xi}^{\xi} dr dr' \frac{e^{i\sigma(r'-r)-\beta^2(r'-r)^2}}{(1+ir)(1-ir')}. \tag{2.41}$$

The maximum of this double integral is reached for $B_m = 0$, $\sigma_m = 0.57$ and

$\xi_m = 2.84$ and is $h(\sigma_m, \xi_m, B_m, \mu = 0, \kappa = 0) = 1.068$. With these definitions and understanding the laser setup in Chapter 3, the SHG processes can be understood.

2.6 Line broadening mechanisms

Absorption or emission of electromagnetic radiation from an atom yields a spectral line frequency that is not monochromatic. Even with an infinitely good experimental resolution, a frequency distribution with a finite width is observed. We define the frequency interval between the two points where the intensity has fallen to half the maximum intensity as the Full Width at Half Maximum (FWHM) of the distribution. Line broadening mechanisms in real atoms can be separated in two classes: homogeneous and inhomogeneous broadening. Homogeneous broadening appears in the form of a Lorentzian profile. Inhomogeneous broadening on the other hand, with Doppler broadening as a primary example, shows a Gaussian line profile. In the following we will discuss contributions to the line broadening of an atomic transition.

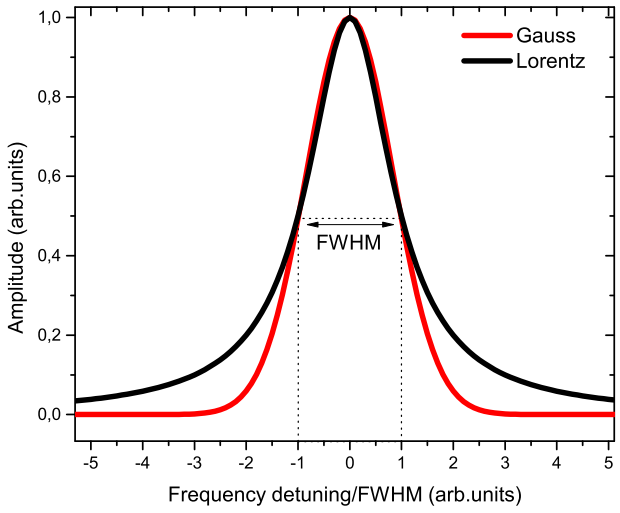

Figure 2.8: Comparison of a Lorentzian and a Gaussian line profile with the same FWHM and the same amplitude.

2.6.1 Natural linewidth

According to Heisenberg's uncertainty relation, the finite life time of an excited state is linked to an uncertainty in the transition energy. The finiteness of the lifetime of an excited state is due to spontaneous emission, caused by quantum fluctuations. The Lorentzian profile of the natural linewidth can be obtained by using the model of a damped harmonic oscillator. The Fourier transform of the oscillation amplitude yields the spectral intensity distribution. The resulting profile

$$I(\omega) = I_0 \cdot \frac{\gamma/2\pi}{(\omega - \omega_0)^2 + (\gamma/2)^2} \tag{2.42}$$

is, as mentioned above, a Lorentzian profile with a FWHM=γ, where γ stands for the natural linewidth, ω_0 for the resonance frequency and I_0 for $\pi/2$ of the maximum intensity.

2.6.2 Saturation intensity and power broadening

The high intensities that can be achieved by lasers induce another form of homogeneous broadening called saturation broadening. We consider a homogeneously broadened 2-level system with a ground level population of N_1 and an excited level population N_2. The rate equation of the upper state population N_2 is then given by:

$$\frac{dN_2}{dt} = -W(N_2 - N_1) - \frac{N_2}{\tau} \tag{2.43}$$

where $W = \sigma F = I/h\nu$ is the single atom transition rate and τ is the lifetime of the excited state. This function is given by

$$N_2 = \frac{1}{2}(N_t - \Delta N), \tag{2.44}$$

with $N_t = N_1 + N_2$ and $\Delta N = N_1 - N_2$. Differentiating 2.44 we get

$$\frac{dN_2}{dt} = \frac{d}{dt}\left(\frac{1}{2}(N_2 - \Delta N)\right) = -\frac{1}{2}\frac{d\Delta N}{dt}, \tag{2.45}$$

since $dN_t/dt = 0$. Setting this result equal to the result of equation 2.43 we get

$$\frac{d\Delta N}{dt} = -\Delta N \left(\frac{1}{\tau} + 2W\right) + \frac{N_t}{\tau}. \tag{2.46}$$

In a steady state , which is the case when the light of a continuous wave (cw) laser is absorbed, $\frac{d\Delta N}{dt} = 0$ and equation 2.46 becomes

$$\Delta N = \frac{N_t}{1 + 2W\tau}. \tag{2.47}$$

The power absorbed per unit volume equals the absorptions per unit time per unit volume times the energy loss per absorption:

$$\frac{dP}{dV} = W \cdot \Delta N \cdot \hbar\omega = \hbar\omega \frac{N_t W}{1 + 2W\tau}. \tag{2.48}$$

We define the saturation intensity as $I_{\text{sat}}(\omega) = h\nu/2\sigma\tau$ and obtain

$$\frac{\Delta N}{N_t} = \frac{1}{1 + \dfrac{I}{I_{\text{sat}}}}. \tag{2.49}$$

The minimum value of I_{sat} occurs for the highest σ. This value is given by [40]

$$I_{\text{sat}}(\omega_0) = \frac{\pi}{3}\frac{hc}{\lambda^3\tau}. \tag{2.50}$$

From equation 2.46 we can easily verify that a laser intensity of $I = I_{\text{sat}}$ leads to a population distribution $N_1 = 3N_2$. For very high intensities $N_1 = N_2$, which means that the absorption coefficient goes to zero. The absorption coefficient line profile is given by a Lorentzian function

$$\alpha_s(\omega_0) = \frac{(\gamma/2)^2}{(\omega - \omega_0)^2 + (\gamma_s/2)^2}, \tag{2.51}$$

where

$$\gamma_s = \Delta\omega_{FWHM} = \gamma \left(1 + \frac{I}{I_{\text{sat}}}\right)^{1/2}. \tag{2.52}$$

is the new linewidth. In conclusion, considering the saturation intensity, we obtain a Lorentzian profile again, however the linewidth γ_s is larger than the natural linewidth γ. The linewidth increases with a square root dependence with the intensity. This type of broadening is called power broadening or saturation broadening.

2.6.3 Doppler broadening

Atoms have, in addition to their internal oscillations, a thermal or Brownian motion, with a Maxwellian distribution of velocities. When an atom moving with a velocity v_z interacts with a photon of frequency ω and velocity c along the z direction, the atom will see the frequency of the wave as:

$$\omega' = (1 - v_z/c) \cdot \omega, \tag{2.53}$$

in accordance with the Doppler effect. This means that the resonance frequency of the light ω_0, normally without a Doppler effect will be Doppler shifted to a new value

$$\omega_{0'} = (1 + v_z/c) \cdot \omega_0. \tag{2.54}$$

The Maxwell frequency distribution for the number of atoms per unit volume in the state i that absorb or emit between ω and $\omega + d\omega$ is given by

$$n_i(\omega)d\omega = \frac{c \cdot N_i}{\omega_0 \cdot v_w \cdot \sqrt{\pi}} \exp - \{c(\omega - \omega_0)/(\omega_0 \cdot v_w)\}^2 d\omega, \tag{2.55}$$

where $v_w = \sqrt{2k_BT/m}$ is the most probable velocity, N_i is the total number of atoms in the absorbing state E_i per volume unit and c is the speed of light. Since the radiation power $P(\omega)$ is proportional to $n_i(\omega)$, the Doppler broadened line profile will have the form:

$$P(\omega) = P(\omega_0) \cdot \exp\left\{-\left[c(\omega - \omega_0)/(\omega_0 \cdot v_w)\right]^2\right\} d\omega. \tag{2.56}$$

This is a Gaussian shaped line with a FWHM of

$$\delta\omega_D = 2\sqrt{ln2} \cdot \omega_0 \cdot v_w/c \tag{2.57}$$

which is for an uncollimated gas with $u_w = \sqrt{\frac{2k_BT}{m}}$

$$\delta\omega_D = (\omega_0/c)\sqrt{(8k_BT \cdot ln2)/m} \tag{2.58}$$

However, for a collimated beam the most probable velocity becomes $v_w = \sqrt{\frac{3k_BT}{m}}$ and therewith equation 2.57 becomes

$$\delta\omega_D = (\omega_0/c)\sqrt{(12k_BT \cdot ln2)/m}. \tag{2.59}$$

A useful formula to estimate the (frequency) Doppler width $\nu = \omega/2\pi$ is

$$\delta\nu_D = 7.16 \cdot 10^{-7}\nu_0 \cdot \sqrt{T/M}s^{-1}, \tag{2.60}$$

with M the atomic mass number. Figure 2.8 represents a comparison of a Lorentzian and a Gaussian line profile. The Doppler contribution to the linewidth is usually much larger than the natural linewidth contribution. This makes it almost impossible to draw conclusions about the natural linewidth. However, as can be seen in figure 2.8, the Gaussian profile power $P(\omega)$ decreases much faster than for the Lorentzian profile with increasing detuning. This is what makes it possible to experimentally gain information about the natural linewidth from the outer tails of the Lorentzian distribution.

2.6.4 Other broadening mechanisms

Transition time broadening

The interaction time of atoms with the laser beam can be short compared to the decay lifetime τ, especially in the case of crossed beam experiments. In this case, the transit time T_{tr} limits the duration of the interaction between atoms and light and thus a kind of effective lifetime broadening occurs. This type of broadening is referred to as transit time broadening and is typically in the order of $\Delta\omega = 1/\tau_{tr}$. The thermal velocity of atoms is typically in the range of $\approx 10^5$ cm/s, so that even for the most focused beam, the effect will not exceed a couple kHz in line width. For the experiments carried out during this thesis, the effect of transit time broadening is negligible.

Pressure broadening

Another type of broadening is pressure broadening. Pressure broadening occurs when atoms collide with other atoms of the same or different kind. The collision broadening contribution to the homogeneous line width will then be directly proportional to the gas density. The effect is negligible under the experimental conditions of our apparatus and therefore no further details will be discussed.

3 Experimental setup

This chapter describes the experimental setup used for the measurements following in the next chapter. Figure 3.1 presents a general overview of the main experimental setup. At the bottom, the beryllium oven is depicted, essentially consisting of a small aluminum oxide (Al_2O_3) crucible wrapped by a resistively heated tungsten wire (see figure 3.2 and A.1. In the center, the main interaction chamber is presented, where the 235 nm UV laser beam meets the hot, vaporized beryllium atoms and produces Be^+ ions. The main chamber contains a set of electrodes that can

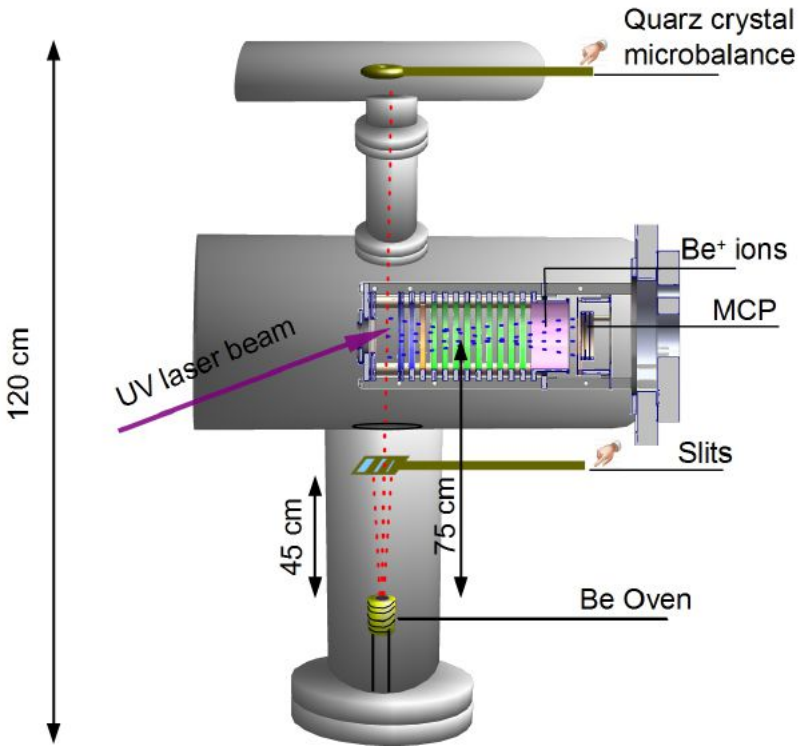

Figure 3.1: Experimental setup.

be set on potentials of 0-200 V in order to focus and accelerate the produced Be^+

ions toward or away from a detector. The main acceleration potential difference however is next to the front surface of the Micro Channel Plate (MCP) detector at the end of the set of electrodes which is held at a potential of −2.1 kV. Additionally, a quartz crystal microbalance detector was installed in order to determine the flux of the evaporated Be atoms. The detector was initially installed between beryllium oven and interaction region, but was later placed behind the interaction region, in order to determine the actual flux in the interaction region. Finally, a set of slits of variable width was inserted, allowing to study Doppler shift effects.

3.1 Oven design and operation geometry

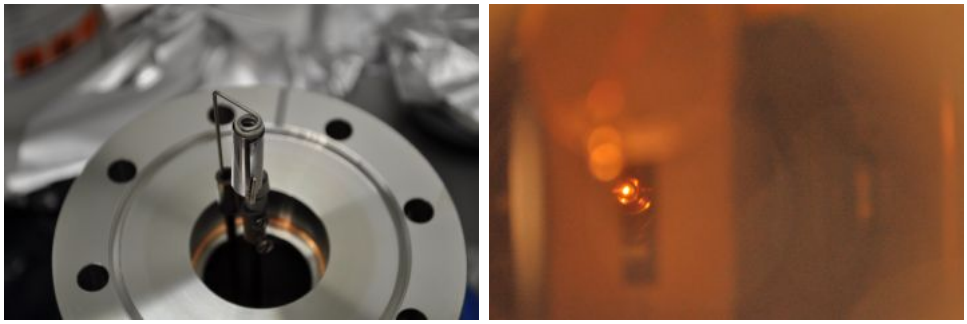

(a) The Be oven before installation

(b) View of the oven from the top of the setup. A slit of 2 mm is visible.

Figure 3.2: Be oven pictures.

In order to vaporize beryllium, an oven had to be constructed that can reach temperatures close to the melting temperature of beryllium (1358 K). Several attempts were carried out in order to find an optimized setup. Reaching such high temperatures turned out to be less trivial than expected. In particular, considerations about the toxicity of Be obliged us to avoid tests with the material itself. The material used for the tests was copper, a metal with a slightly lower melting temperature than beryllium (1358 K). The tests showed that copper was melted after the test, which proves that a temperature of at least 1358 K was reached at an operating current of 11 A and electrical power of 26.5 W. The material used for the crucible was, as mentioned above, Al_2O_3, a ceramic designed to withstand temperatures up to at least 1750 K. Wrapped around the oven is a tungsten filament (melting point

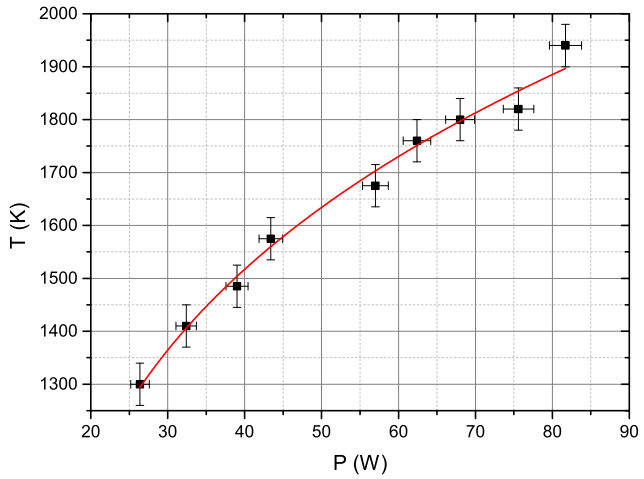

Figure 3.3: Temperature-power diagram. A fourth root fit has been made for the data points. The reading error for the temperature is estimated to $\Delta T = 40\,\mathrm{K}$.

3683 K), ordered as a custom-built model from *Midwest Tungsten Filaments*, that is directly connected to an electric power source. In order to minimize the radiation heat loss of the oven, additional layers surround the filament. The first layer is a tube of Al_2O_3 and wrapped around it, a thin sheet of tantalum mounted with clips that are made out of titanium wire. Tantalum and titanium have been chosen first because of their very high melting temperatures and second because of their physical properties. Tantalum is a very ductile metal while titanium is strong and once formed it is very hard to be deformed. All these components can be viewed on figure A.1 in the Appendix.

The melting temperature of beryllium is 1560 K but such a high temperature does not necessarily have to be reached for our purpose, since the sublimation rate is significant and sufficient at lower temperatures. All final experiments were performed at a current of (13-14) A and a power of about 40 W so the estimated temperature was estimated to about $(1500 \pm 40)\,\mathrm{K}$. Another way to determine the temperature of the oven is by using a pyrometer, a device with which the color of the investigated light source can be compared with a temperature-calibrated internal light source and the temperature can be deduced. Since the accuracy of this method is limited by how exact the eye can compare the two light source colors

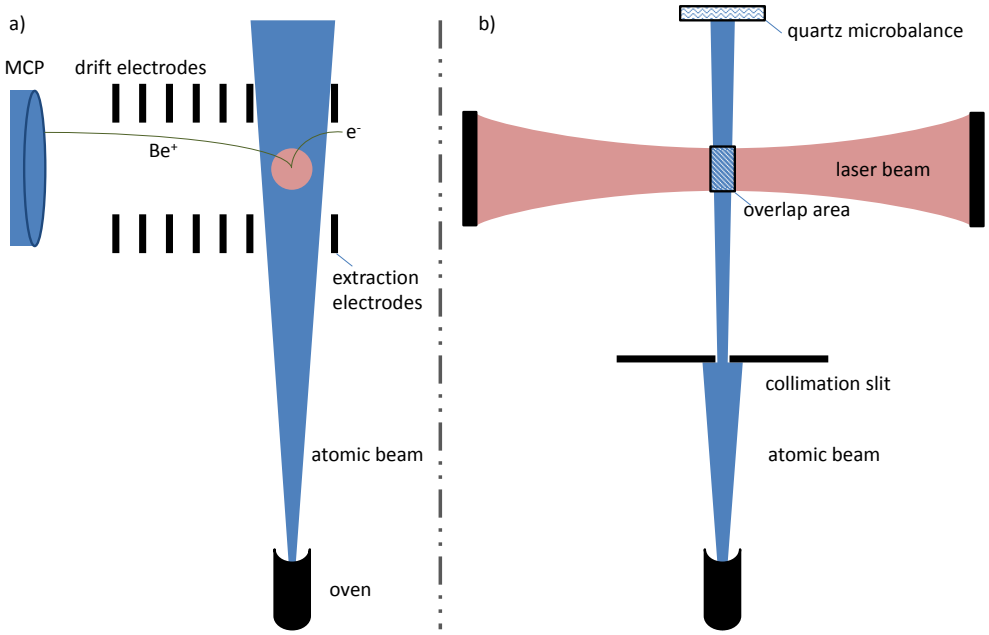

Figure 3.4: Schematic view of the experiment. (a) Side view. Be^+ ions are accelerated to the MCP detector while free electrons are pushed away. (b) Front view. The focused laser beam and collimated atomic beam overlap at the interaction region.

with each other, the apparatus has an estimated uncertainty of about 40 K. On figure 3.3, a graph of the applied electric power versus the estimated temperature is presented. A fourth root dependence can be observed as expected. The radiation power is given by the Stefan Boltzmann rule $P_{rad} = \sigma T^4$ where σ is the Boltzmann constant. If P_{el} is set equal to P_{rad}, a fourth root dependence of the temperature on the power is found. In order to decide what an adequate temperature for the oven is, the sublimation rate (that indicates the rate of atoms) can be calculated. At a temperature T the sublimation rate is given by the Hertz-Knudsen equation [39].

$$\frac{dn}{dt} = \frac{\alpha}{\sqrt{2\pi MRT}} \cdot S \cdot P_D(T) \tag{3.1}$$

Here α is the sticking coefficient, R is the ideal gas constant, M the molar mass, S the free surface of the oven and $P_D(T)$ the vapor pressure [10] at temperature T. We calculate for instance the sublimation rate at a temperature of $T = 1480\,\mathrm{K}$ (corresponds to our operating current of 13 A.). The oven has an opening of $S = 2\,\mathrm{mm}^2$, the molar mass of beryllium is $M = 9.02\,\mathrm{g/mol}$ and the vapor pressure at

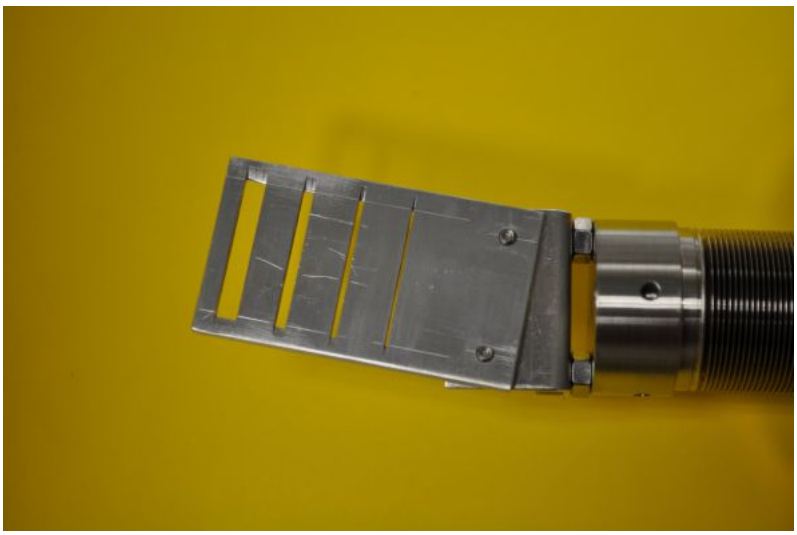

Figure 3.5: Visible are the four slits with dimensions(from left to right 4,2,1 and 0.6 mm)×20 mm mounted on a translation stage. The slits are inserted under an angle, since the flange where it is meant to be installed also has an angle corresponding to the laser beam. This angle is crucial for Doppler effect measurements (See Section 4.1.

that temperature is about $P_D(1480\,K) = 1\,\mathrm{Pa}$ [21]. Thus, the sublimation rate assuming $\alpha = 14$ is $dn/dt = 7.58 \cdot 10^{-8}\,\mathrm{mol/s}$ and therewith the vaporization rate of atoms is calculated to about $4.56 \cdot 10^{16}$ atoms/s or $0.68\,\mu\mathrm{g/s}$.

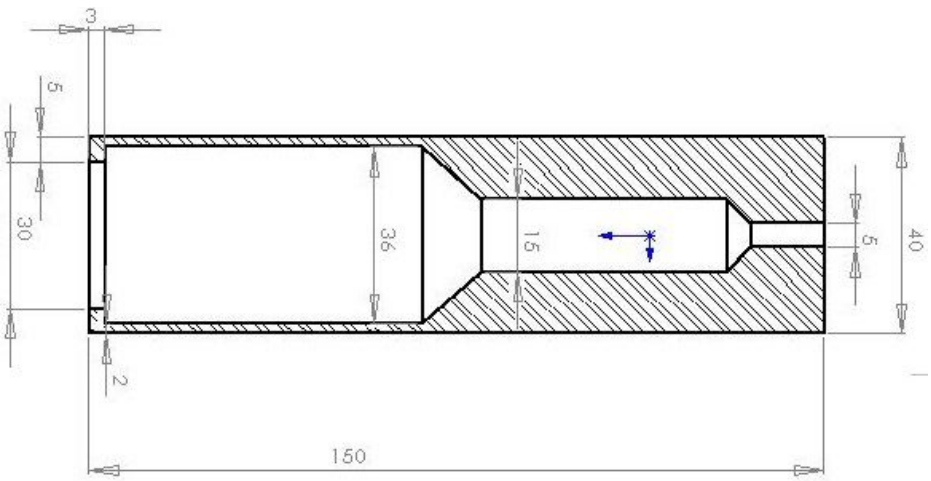

Figure 3.6: Oven cover and dimensions.

3.1.1 Handling beryllium: safety measures

Considerations about the toxicity of Be imposed the use of very small quantities of the metal, and the implementation of several safety measurements. Especially an exposure to airborne beryllium [17] exceeding the occupational standard can cause a chronic lung disease named berylliosis. Ingesting beryllium on the other hand has not yet proven hazardous. Since we are dealing with beryllium in this experiment both in its solid and gaseous form special care is required. The permissible exposure limit (PEL) according to the Occupational Safety & Health Administration (OSHA) rules is $0.02\,\mathrm{mg/m^3}$. The quantity that was placed into the oven was about 11 mg at a time. The vaporization rate estimated by the quartz crystal microbalance is in the order of $3 \cdot 10^{-3}\,\mu\mathrm{g/min}$ for a sensor surface of $0.539\,\mathrm{cm^2}$. Thus, for a solid angle of 2π, this corresponds to a mass of about $72\,\mu\mathrm{g/min}$. In order to direct the beam of vaporized atoms to the interaction region without seriously contaminating the chamber walls, a cover for the oven was built. The design of the cover is shown on figure 3.6. It consists of an aluminum tube of gradually decreasing inner radius. The oven is positioned inside the aluminum tube at a 5 cm distance from the side with the large opening. The calculated solid angle where beryllium can spread is then a factor $2.4 \cdot 10^{-3}$ smaller than the 2π angle, which leads to a vaporization rate of two magnitudes less, namely $3 \cdot 10^{-2}\,\mu/\mathrm{min}$. For an approximate duration of 20 hours in which the experiments were done, an amount of approximately $36\,\mu\mathrm{g}$ are expected to be vaporized. Other measures have also been taken in order to minimize health risks of the toxic metal. In order to avoid potential beryllium concentration in the laboratory, the outgoing air from the vacuum pumps is transported outside the building. While handling with beryllium in its solid state, all required safety measures were taken such as using gloves, safety glasses and respiratory masks. A sturdy plastic bag was held under the chamber when beryllium had to be installed so that potential dust would be collected and disposed properly. For further information about dangers of beryllium and necessary measures to be taken when working with the metal see Appendix C.

3.2 Vacuum and optical arrangement

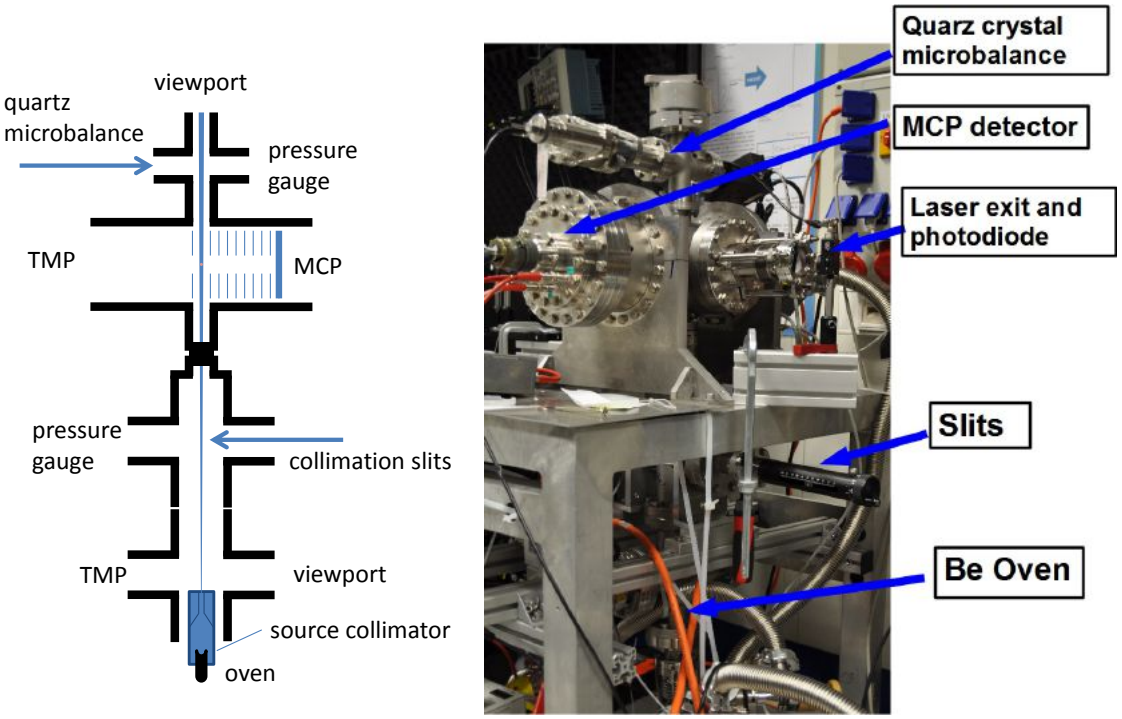

(a) Scheme of the experimental setup (b) Photograph of the real experimental setup with the main elements labeled.

The experimental setup consists of one main ConFlat (CF) vacuum chamber with a diameter of 200 mm, two CF 63 mm diameter crosses below the main chamber where the oven and variable slits are installed (see figure 3.5 and a CF 40 mm T-shaped chamber on the top with an extension for the quartz crystal microbalance. The chambers also have various exits where two 80 l turbomolecular vacuum pumps and two pressure gauges are attached. In order to minimize the count rate originating from the direct laser light on the MCP detector, two aluminum tubes were constructed. As is visible in figure 3.7, the two tubes are adjusted to the main chamber for the entrance and one for exit of the laser light. The reflection inside the tubes was minimized by making sure that the internal tube surfaces are rough and thus largely only diffusely reflecting. As depicted in picture 3.8, there is an optical setup on the left hand side of the main chamber, before the window where the laser light enters the chamber. It consists of suitable custom anti-reflection coated (Layertec) mirrors directing the beam, one adjustable aperture and a focus-

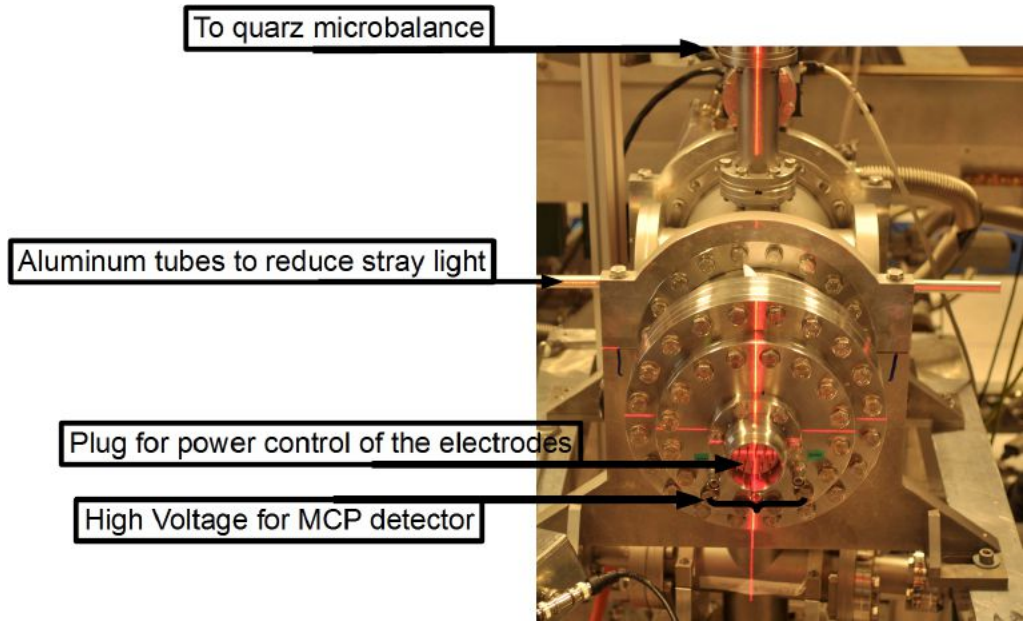

Figure 3.7: Alignment of the two stray light reducing tubes with a crossed alignment laser.

ing lens (f=500mm, Thorlabs LA4184 UV Fused Silica Plano-Convex). The lens is removable and is only used for a part of the experimental time in order to study its influence on saturation effects and ion yield.

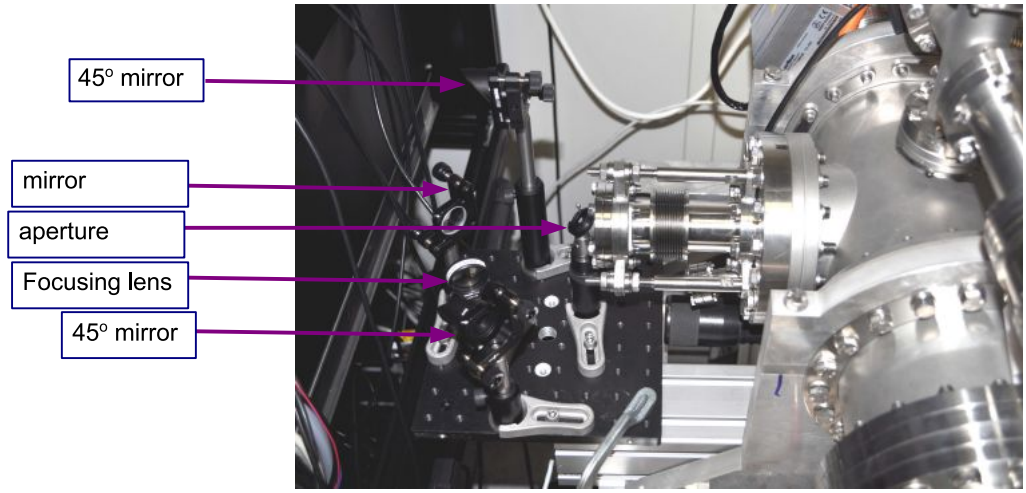

Figure 3.8: Optics before the entrance to main vacuum chamber. Three mirrors (one of them on a 45° mount), a focusing lens and an aperture can be seen.

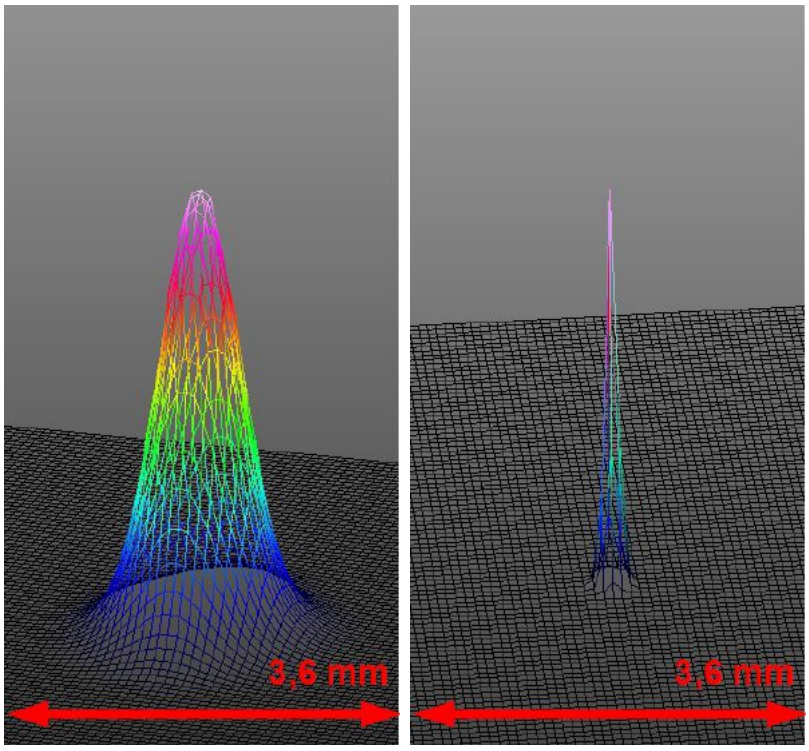

(a) Beam profile without focusing lens.

(b) Beam profile with focussing lens.

Figure 3.9: Optical beam profiler pictures. Comparison of beam profiles with and without a focusing lens with focus at f=500 mm.

The laser beam was characterized and the beam width was measured with a scanning slit optical beam profiler from Thorlabs (Model BP209-VIS). The resulting 3D images of the beam at a distance that corresponds to the interaction center with and without the usage of the focusing lens are showed on figure 3.9. The beam profile diagrams with and without the focusing lens are shown on figures 3.10 and 3.11. A Gaussian function is fitted showing that the beam is in a good approximation a Gaussian beam.

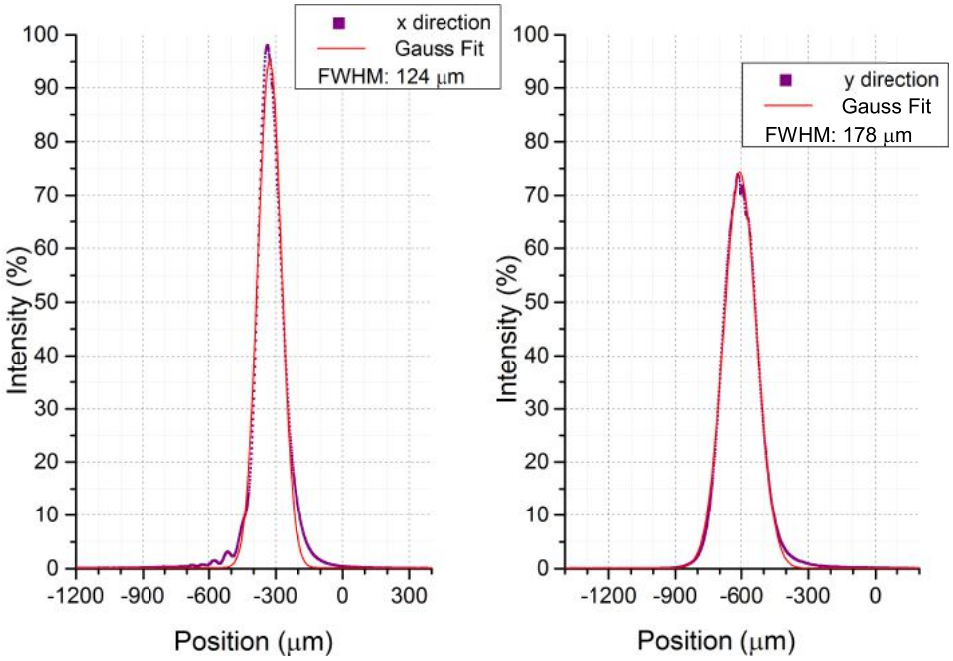

Figure 3.10: Beam spread in x and y directions when a focusing lens with f=500 mm is used.

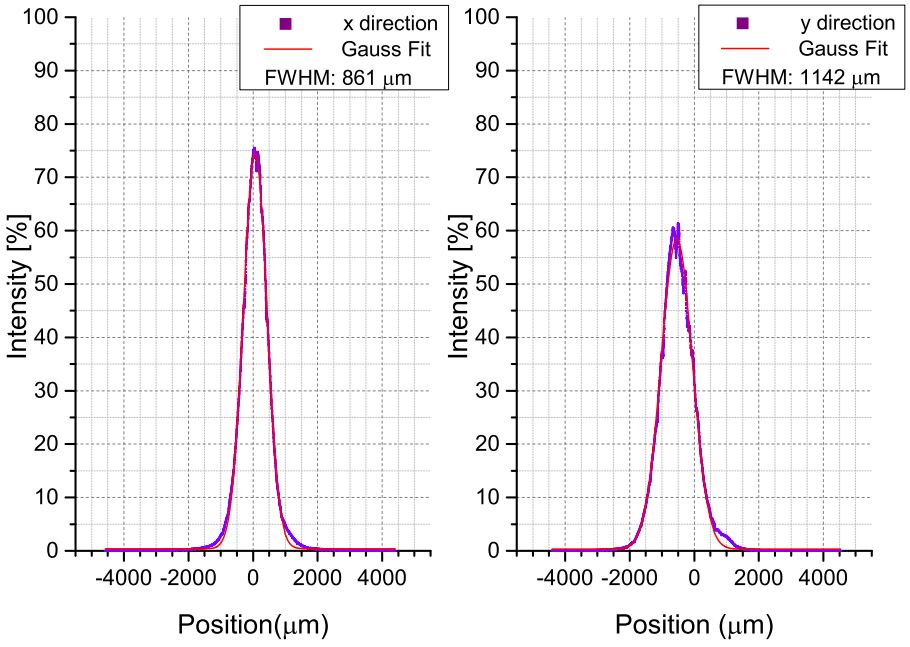

Figure 3.11: Beam spread in x and y directions when no focussing lens is used.

3.2.1 Photoionization laser

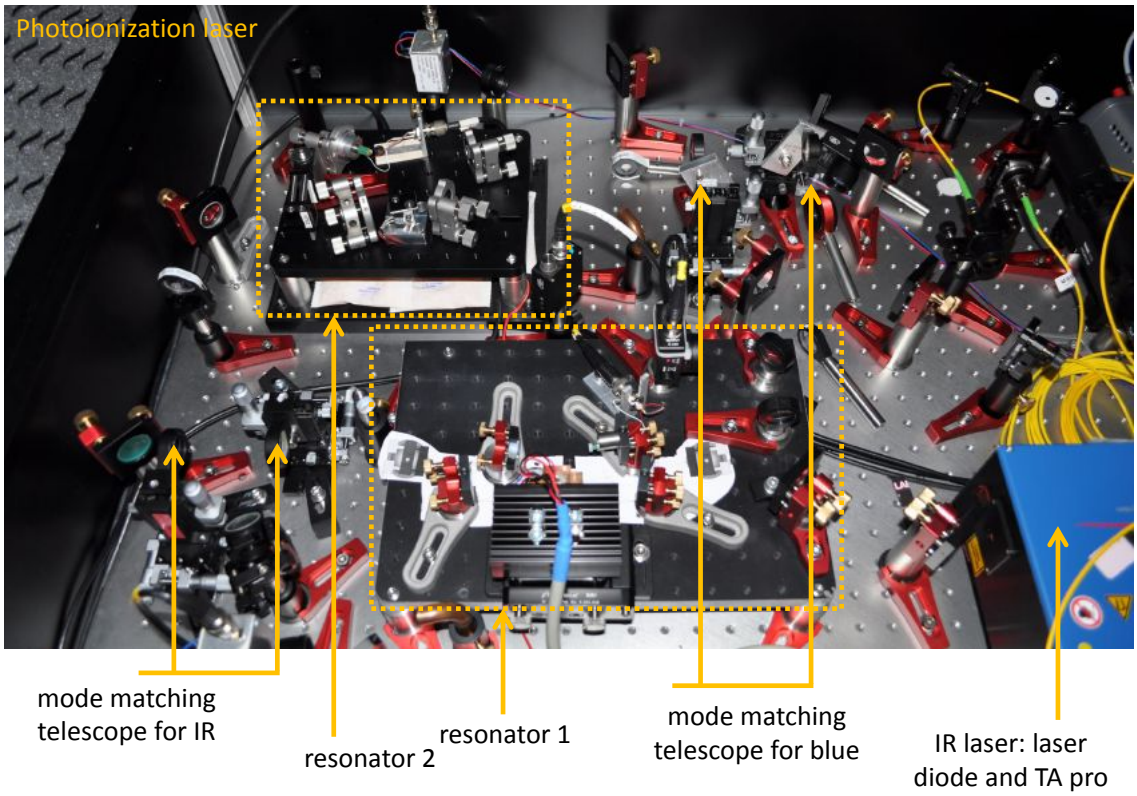

Figure 3.12: Picture of the laser setup. In the foreground the first resonator converting IR light into blue light is seen. In the background to the left the second resonator that converts blue light into UV light is seen.

In order to ionize beryllium, an energy of about 9.3 eV is required, corresponding to a wavelength of about 133 nm. Since this wavelength is very hard to generate with a laser, a resonance enhanced two-photon process is chosen instead. This process requires using a laser source at 235 nm, which corresponds to the transition $1s^2 2s^2\ {}^1S_0 \rightarrow 1s^2 2s 2p\ {}^1P_1$ at 5.27 eV. Such a wavelength is also difficult to produce. The laser system has been constructed in cooperation with PTB. It is based on frequency quadrupling the light of a commercial diode laser acquired with a tapered amplifier (TA). The laser source is a commercial Toptica 940 nm diode laser that can provide up to 1500 mW output power. The figure below shows the setup of the laser system. It consists of mirrors (M), lenses (L), λ plates, an optical isolator to prevent damage to the TA and diode laser from back-reflected laser light at the beginning.

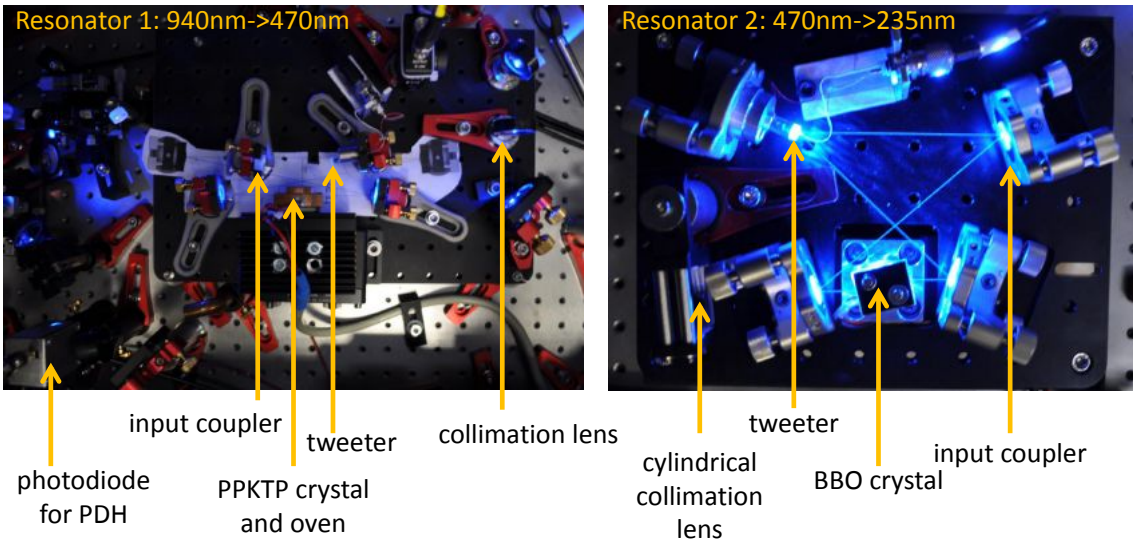

Figure 3.13: Picture of the laser setup. In the foreground the first resonator converting IR light into blue light is seen. In the background to the left the second resonator that converts blue light into UV light is seen.

First SHG stage

Thermal lensing issues limit the efficiency of the first second harmonic generation (SHG) stage, based on resonance enhanced doubling in a bow-tie cavity using an AR-coated PPKTP crystal. This type of crystal has been chosen because of its high non-linearity and transparency at both 940 nm and 470 nm. It is held at a stabilized temperature of about 21°C during laser operation for quasi phase matching. The length of the cavity is locked to the laser using the Pound-Drever-Hall (PDH) technique [32] . PDH locking offers a solution to various fluctuations by actively tuning the laser to match the resonance frequency condition of a cavity. Essentially the technique can be described as follows. First, light that is reflected off the cavity is measured by using a high-speed photodetector, a signal that consists of two unchanged side bands and one phase shifted component. Then the light is mixed down with a phase shifted oscillator and is then low pass filtered. The electronic signal that results is then fed into the laser and gives a measure of how far off resonance the laser frequency is. The geometry of the cavity has been optimized to reach high conversion efficiency by trying out three different arrangements. The maximum output power of the resonator at an input laser current of 2157 mA was about

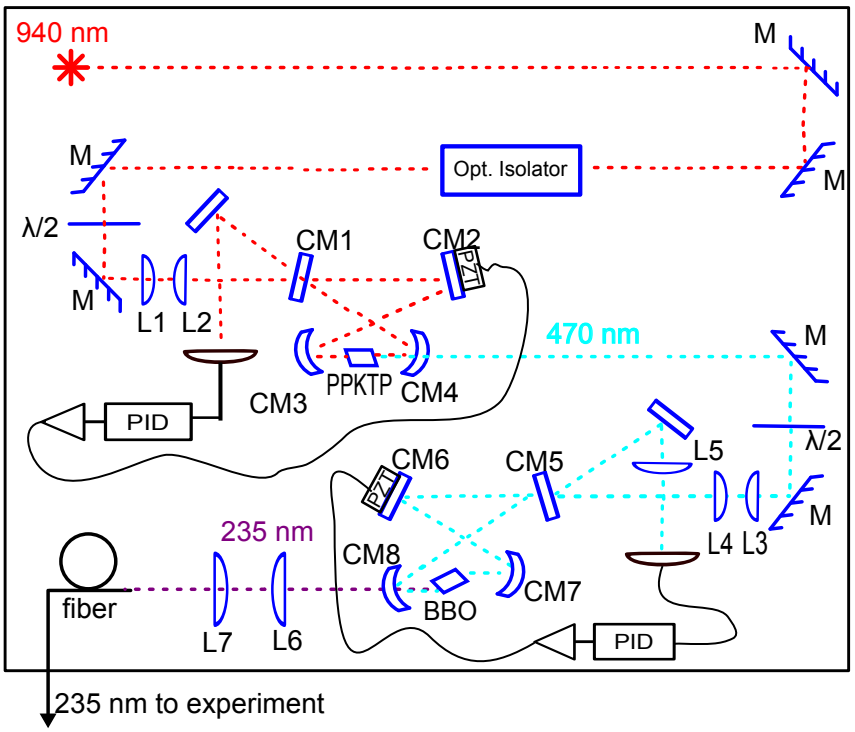

Figure 3.14: Photoionization laser setup.

300 mW. The value for the Boyd-Kleinman focusing parameter is $\xi = l/b = 2.84$ where l is the length of the crystal and $b = 2\pi n\omega^2/\lambda$ the confocal parameter of the laser beam. Our PPKTP crystal has a length of $l = 20\,\text{mm}$. Table 3.1 contains other useful characteristics of the crystal. With the help of the values in table 3.1 we can calculate the Boyd-Kleinman factor h. A Faraday isolator prevents damage to the TA and diode laser from back-reflected laser light for both fundamental and harmonic waves. As already mentioned, the ideal focus position is the center of the crystal where $\mu = 0$. According to 2.39 and equation 2.41 the maximum value of h is

$$h(\sigma, B, \xi) = 1.0677 \tag{3.2}$$

The resulting outgoing power is then calculated according to 2.38 and is for an incoming power of $P_0 = 1\,\text{W}$, $P_1 = 36.9\,\text{mW}$. The conversion efficiency then results to

$$K = \frac{P_1}{P_0^2} = 0.037\,\text{W}^{-1}. \tag{3.3}$$

Characteristic	**Abbreviation**	**Value**
crystal length	l	20 mm
fundamental wavelength	λ_1	940 nm
SHG wavelength	λ_2	470 nm
nonlinear coefficient	$\chi_{(2)}$	$9.9 \cdot 10^{-12}\, m/V$
walkoff	ρ	$0.1 \cdot 10^{-3}$ rad
refractive index for λ_1	$n_C^{(1)}$	1.835165
refractive index for λ_2	$n_C^{(2)}$	1.9138
absorption for λ_1	α_1	$0.3\, m^{-1}$
absorption for λ_2	α_2	$14\, m^{-1}$
grating period	Λ	$5.977\, \mu m$

Table 3.1: Characteristics of the PPKTP crystal. Taken from SNLO software.

For the rest of the calculated optimal parameters see table 3.2. The actual power output of the cavity however is much larged due to resonance enhancement. The actual power in the ideal case is calculated to 380 mW.

parameter	**Value**
ξ	2.84
ω_0	23.96 μm
k_1	$12.26 \cdot 10^6\, m^{-1}$
b	0.007 04 m
Δk	162.822 m^{-1}
σ	0.57

Table 3.2: Parameters of the PPKTP crystal for optimal conversion efficiency.

Second SHG stage

The second SHG system also relies on resonance enhanced doubling in a bow-tie cavity employing a Brewster-cut BBO crystal this time. Here critical type I phase

matching is used. In contrary to the first stage, here a nonzero walk-off is induced because of the of the use of angle phase matching. This walk-off limits the length of the crystal where conversion takes place. A 10 mm crystal was chosen. The PDH method is here also used to keep the length of the cavity on resonance with the CW laser. The maximum achieved output power of the 235 nm wavelength light by a 470 nm input power of 300 mW was about 30 mW. Table 3.3 contains all necessary information about the BBO crystal.

Characteristic	**Abbreviation**	**Value**
crystal length	l	10 mm
fundamental wavelength	λ_1	470 nm
SHG wavelength	λ_2	235 nm
nonlinear coefficient	$\chi_{(2)}$	$1.48 \cdot 10^{-12}$ m/V
walkoff	ρ	$79.78 \cdot 10^{-3}$ rad
refractive index for λ_1	$n_C^{(1)}$	1.681
refractive index for λ_2	$n_C^{(2)}$	1.681
absorption for λ_1	α_1	$0.4\,\mathrm{m}^{-1}$
absorption for λ_2	α_2	$0.4\,\mathrm{m}^{-1}$

Table 3.3: Characteristics of the BBO crystal. Taken from SNLO software.

parameter	**Value**
ξ	1.5
ω_0	$17.224\,\mu$m
k_1	$22.46 \cdot 10^6\,m^{-1}$
b	0.006 66 m
Δk	$210\,\mathrm{m}^{-1}$
σ	0.7

Table 3.4: Parameters of the BBO crystal for optimal conversion efficiency.

As done for the first cavity, the Boyd-Kleinman factor can also be calculated for

this SHG stage according 2.39 and 2.41 and the maximum value of h results to

$$h(\sigma, B, \xi) = 0.03734. \tag{3.4}$$

This means, for an incoming power of $P_1 = 300\,\mathrm{mW}$ we have $P_2 = 0.015\,\mathrm{mW}$ and therewith a conversion efficiency of

$$K = \frac{P_2}{P_1^2} = 1.65 \cdot 10^{-4}\,\mathrm{W}^{-1} \tag{3.5}$$

The rest of the calculated optimal parameters are seen on the table below. Of course the total UV light power is much higher than the output of one single path through the resonator. The total power after light enhancement in the cavity is calculated to 38.5 mW.

3.3 Ion and fluorescence counting system

Acceleration and drift electrodes

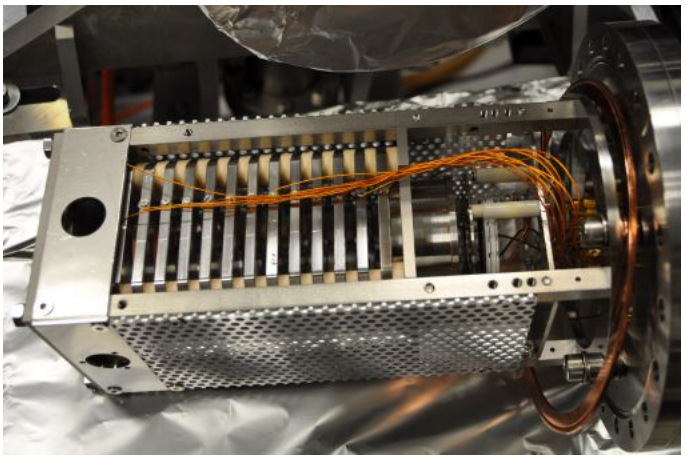

Figure 3.15: Photograph of the set of electrodes and MCP detector used to accelerate the Be^+ ions. More details about the setup found in [38].

The main chamber of the setup contains, as mentioned, a set of stainless steel plates that can be set on potentials in order to accelerate positive ions towards the MCP detector or decelerate them and avoid their detection if required. The setup was built by P. Mrowczynski in his Diploma thesis [38]. A closer view of this

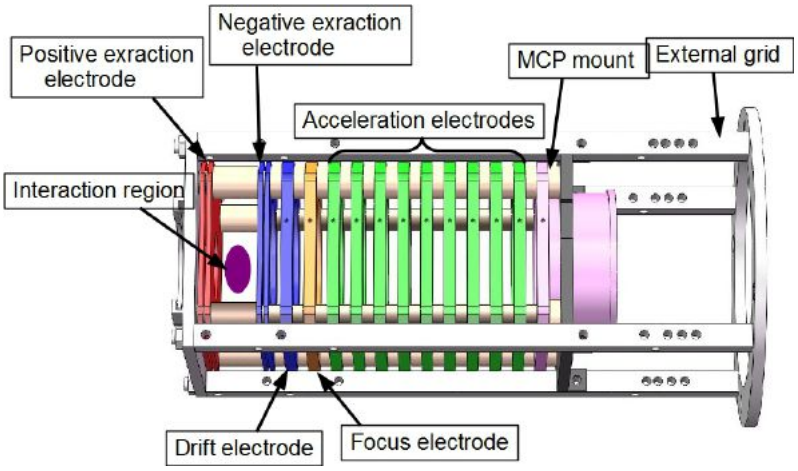

Figure 3.16: Schematic view of electrode construction of the time of flight spectrometer. Modified from [38].

construction is given in figure 3.16 taken from his thesis. Since not every electrode has to be controlled individually, a voltage divider was built that allows operation of the whole set of electrodes with just two power supplies. One of them is responsible for the extraction and focusing of the ion beam and the other controls the rest nine acceleration electrodes. The electrical plan of the voltage divider is presented in the Appendix in figure B.1. Moreover, a simulation of the Be^+ ion trajectory is presented on figure

Micro Channel Plate detector

At one end of the set of electrodes a micro channel plate (MCP) detector is installed. The model used is the MCP-33-D-R-A (tectra GmbH). This type of MCP detector is ideal for our purpose because of its high detection efficiency and its compact size (44 mm diameter and 11 mm thickness). MCP detectors are generally made of one to three semiconductor material plates composed of many small channels of a couple of μm diameter that are arranged in a strainer-like structure. The channels are placed in an angle of about 8° and create a cascade of electrons when a particle hits them, according to the principle of secondary electron emission. In order to increase the number of secondary electrons and therewith the measured current, more MCP plates are placed behind one another. Here two MCP detectors are used In order to detect the ions, a high potential is required to be applied on the front

area of the MCP detector, in this setup 2.1 kV on the first and about 1.7 kV on the second MCP.

3.4 Electronic components for ion detection and MPA system

The signal in all of the following experiments is derived from MCP pulses. These pulses are read out over the anode of the MCP detector and fed into a constant fraction discriminator (LeCroy OD 623B). The resulting NIM pulses are then converted to TTL standard and fed into the MPA3 (FastCOMTECH) data acquisition system as a systems trigger input. A voltage ramp of triangular shape, provided by a function generator(Agilent 33220A), gives a time reference. Together with the trigger input a histogram of MPC count versus time is constructed. Furthermore, a voltage signal from a photodiode is fed into the MPA system to track UV laser power fluctuations. The laser frequency is scanned through the SCAN module of the Toptica control electronics. This module scans both piezo voltage and laser diode current in such a way that output power is rather constant, and scan range is maximized. The laser frequency is scanned with a sawtooth voltage output from a second function generator, the SYNC output of which is also fed into the MPA system to provide a readout of the start of one of such linear scans. A phase offset of 60 degrees, between start scan and SYNC TTL, was found to be present and had to be corrected in the off-line data analysis.

3.5 Calibration with a quartz crystal microbalance

In order to accurately measure the atomic flux, a very precise quartz crystal microbalance detector was used (Model STM-2XM from sycon instruments). According to the manufacturer it has a $0.002\mathring{A}$ thickness Resolution per measurement(for 50 measurements averaged). During the experiments, this instrument was used for the estimation of the density rate of vaporized beryllium. This estimation is required both for comparison with potentially dangerous beryllium levels and for estimating the photoionization cross section according to Section 4.3.1

4 Experimental results

In this Chapter the experimental results are discussed. First, we discuss line shapes obtained by scanning the laser frequency and monitoring the MCP count rate. Second, we estimate the total cross section of the one and two photon ionization of beryllium using two different models.

4.1 Characterization of the atomic beam

In this Section some effects that are important for the final calculation of the ionization cross section of beryllium are determined. These involve the influence of the Doppler effect that impacts on the position (Doppler shift) and spread (Doppler broadening) of the expected photoionization and fluorescence spectra. These effects are discussed, calculated and compared with the experimental results.

4.1.1 Doppler shift and broadening calculation

In order to estimate the Doppler shift and broadening, the velocity of the Be atoms has to be known. For an uncollimated gas beam, the most probable velocity is $v = \sqrt{2k_BT/m}$. However, for a collimated atomic beam the resulting most probable velocity is higher and equals $v = \sqrt{3k_BT/m}$. In our case, the atomic beam temperature was estimated to be $T = 1490 \pm 40\,\mathrm{K}$ (See Section 3.1 and Figure 3.3) and the atoms have a most probable velocity of approximately $v \approx 2032 \pm 28\,\mathrm{m/s}^2$. A first order Doppler shift only takes place for the component of the atomic beam that propagates parallel to the laser beam. This component has been minimized in this setup since the crossed-beam method was used. The oven and laser beam were very carefully aligned so that the atomic and laser beams propagate at right angles. The estimated error of the crossed alignment laser used here is in the order

of 3 mrad. In this case, the observed Doppler shift given by

$$\Delta f(\theta) = \pm f_0 \cdot \frac{v}{c} \cdot \sin\theta \tag{4.1}$$

would be about 26 MHz for the relevant laser frequency of $f_0 = 1.3 \cdot 10^6$ GHz. If the atomic beam was completely parallel to the laser beam, the Doppler shift would be $\Delta f = 8.6$ GHz. The complete Doppler width can be calculated using equation 2.59, resulting in a width of $w_D = 14.4 \pm 0.2$ GHz. The collimation of the beam, however, has to be taken into account (see figure 3.4). Without a collimation slit, the beam opening angle α is about 30 mrad. By inserting a collimation slit of 2 mm, the opening angle reduces to about 4.4 mrad. This corresponds to a Doppler width reduction to $w'_D \approx w_D \cdot \alpha$ which gives $w'_D = 430$ MHz and $w'_D = 63$ MHz without and with a slit correspondingly.

4.1.2 Results

Figures 4.2 and 4.1 present spectra obtained with three different slit settings. Figure 4.2 presents the combined data of ionic detection and fluorescence detection while figure 4.1 presents only the fluorescence yield with the same settings. In the first case, the acceleration electrode closest to the MCP (blue, see figure 3.16) is put on a -50 V whereas the upstream electrode (red in same figure) is set at +50 V. The resulting electric field guides the ions towards the drift area and thus onto the MCP detector. In the second case, the first acceleration electrode is set to +50 V and the upstream electrode to -50 V resulting in an electric field that guides the ions away from the MCP detector. In this case, only the fluorescence photon yield is counted by the MCP detector. The background counts are primarily a consequence of stray light, that required serious efforts to be minimized. Subtraction of signals, in order to obtain clean ion-only rates, is left to a later section as frequency drifts and possible frequency *shifts* make this procedure non-trivial. All data have been fitted with a Voigt fit, i.e. a convolution of a Gaussian and Lorentzian function. Some spectra have been shifted by a couple of 10 MHz in order to enable comparison of the line widths. This shift could by due to the Doppler shift because of non-perfect alignment. The conclusion that can be drawn from these spectra by comparing the Gaussian contributions to the spectral linewidth, is that the 2 mm slit reduces

significantly the effect of Doppler broadening on the spectrum, compared to the 4 mm slit. Using a 1 mm slit on the other hand mainly reduces the yield of the reacting atoms without reducing the Doppler width significantly.

4.2 Power broadening

In this Section the influence of power broadening on the spectra is studied. As mentioned in Section 2.6.2, high intensities influence the homogeneous line shape of the absorption spectrum. The FWHM of the new Lorentzian form is given by

$$\Delta\omega_{FWHM} = \Gamma\left(1 + \frac{I}{I_{sat}}\right)^{1/2}, \tag{4.2}$$

where Γ is the natural linewidth, I is the intensity and I_{sat} the saturation intensity. The saturation intensity is calculated for this transition according to equation 2.50 and is $I_{\mathrm{sat}} = 8889 \pm 16\,\mathrm{W/m^2}$. The spectra that where studied here, however, are not absorption spectra but either fluorescence spectra or a sum of fluorescence and ionization spectra. Fluorescence spectra are expected to have a similar behavior to absorption spectra. A theoretical description of the behavior of the ionization spectra is, however, harder to give. The absorption spectrum is given by equation [41]

$$I(\omega) = \frac{\hbar\omega}{2\tau}\frac{I_D/4\tau^2}{(\omega-\omega_0)^2 + (I_D+1)/4\tau^2}, \tag{4.3}$$

where $\tau = \Delta\omega_{FWHM}/2\pi$ is the lifetime of the excited level, $\omega - \omega_0$ is the detuning and I_{D} is the intensity in units of the saturation intensity I_{sat}. The shape of the laser beam is in good approximation Gaussian (see Chapter 3.1) so that we can write for the intensity

$$I_{\mathrm{D}} = I_0 \cdot \exp\left[\frac{-r^2}{2\sigma^2}\right]. \tag{4.4}$$

Equation 4.3 thus becomes

$$I(\omega) = \frac{\hbar\omega}{2\tau}\frac{I_0 \cdot \exp\left[\frac{-r^2}{2\sigma^2}\right]/4\tau^2}{(\omega-\omega_0)^2 + (I_0 \cdot \exp\left[\frac{-r^2}{2\sigma^2}\right]+1)/4\tau^2}. \tag{4.5}$$

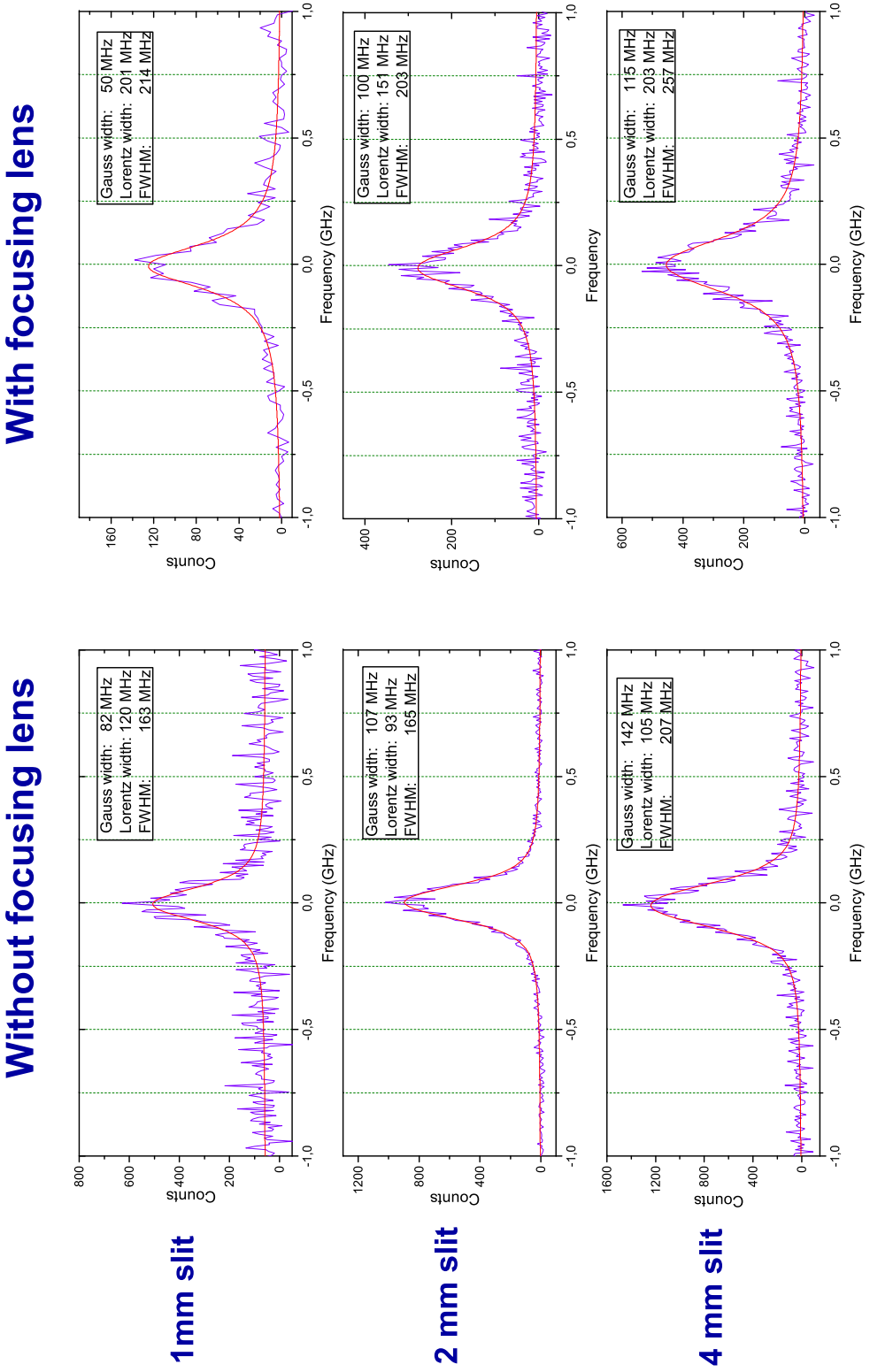

Figure 4.1: Fluorescence peaks for slit widths of 1 mm, 2 mm and 4 mm with and without using a f=500 mm focusing lens. The red line depicts a fit of a Voigt function to the data. A correction to the frequency offset (typically few 10MHz) has been applied in order to set the central frequency at zero. The laser intensity for the spectra with the lens is about $I_{\mathrm{lens}} \approx 4.2 \cdot 10^5\,\mathrm{W/m^2} \approx 47 \cdot I_{\mathrm{sat}}$ and without lens $I_{\mathrm{nl}} \approx 9 \cdot 10^3\,\mathrm{W/m^2} \approx I_{\mathrm{sat}}$.

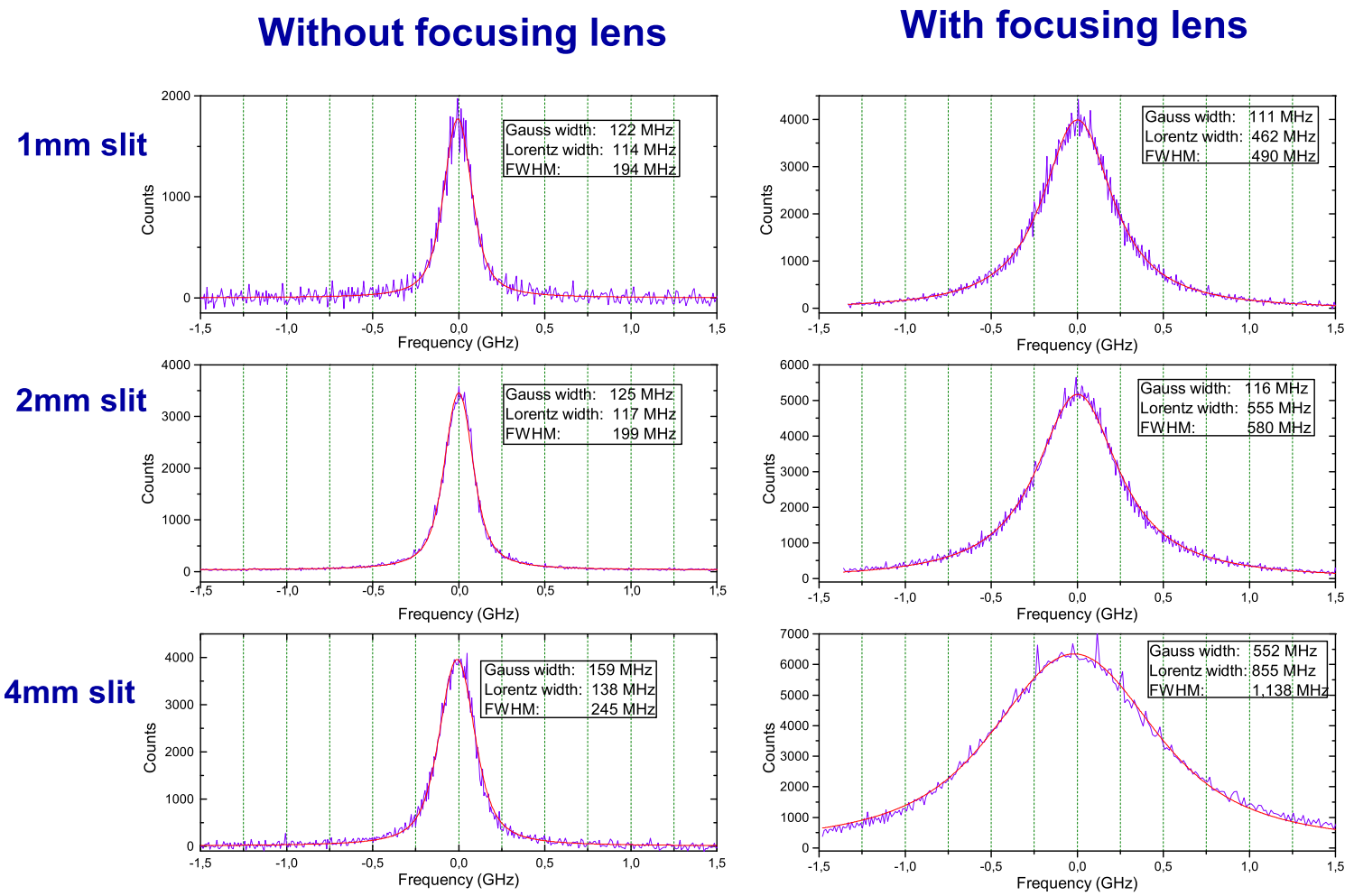

Figure 4.2: Integral photionization peaks, i.e., including fluorescence signal for slit widths of 1 mm, 2 mm and 4 mm with and without using a f=500 mm focusing lens. The red line represents a fit of a Voigt function to the data. A correction to the frequency offset (typically few 10 MHz) has been applied in order to set the central frequency at zero. The laser intensity for the spectra with the lens is about $I_{\mathrm{lens}} \approx 4.2 \cdot 10^5\,\mathrm{W/m^2} \approx 47 \cdot I_{\mathrm{sat}}$ and without lens $I_{\mathrm{nl}} \approx 9 \cdot 10^3\,\mathrm{W/m^2} \approx I_{\mathrm{sat}}$.

Integration of 4.5 over the area of a Gaussian beam yields the form of the resulting fluorescence distribution $I_{\text{fluor}}(\omega)$ according to

$$I_{\text{fluor}}(\omega) = \int \frac{\hbar\omega}{\tau} \frac{I_0 \cdot \exp\left[\frac{-r^2}{2\sigma^2}\right]/4\tau^2}{(\omega-\omega_0)^2 + (I_0 \cdot \exp\left[\frac{-r^2}{2\sigma^2}\right]+1)/4\tau^2} \pi r dr. \tag{4.6}$$

Inserting various values for I_0 in units of the saturation intensity I_{sat}, allows us to determine the expected Lorentzian line widths. In the case of the ion spectrum, the integral that has to be solved in order to obtain the expected intensity distribution is similar to equation 4.6 but has to be multiplied with the laser energy distribution, since each atom has to absorb two photons in order to become ionized. In this case we thus have

$$I_{\text{fluor}}(\omega) = \int \frac{\hbar\omega}{\tau} \frac{I_0^2 \cdot \exp^2\left[\frac{-r^2}{2\sigma^2}\right]/4\tau^2}{(\omega-\omega_0)^2 + (I_0 \cdot \exp\left[\frac{-r^2}{2\sigma^2}\right]+1)/4\tau^2} \pi r dr. \tag{4.7}$$

Figure 4.3 presents the evolution of the spectral line shapes as a function of the applied beam intensity for both photoionization and ion spectra normalized to a amplitude of 1. To good approximation, functions 4.6 and 4.7 are Lorentzian. Deviations from a Lorentzian function become important only at the highest of intensities ($100 \cdot I_{sat}$). The representation of figure 4.3 shows that at low intensities the line shapes are very similar for both the ion and the fluorescence spectra. For higher intensities, the two show stronger disimilarities since the width of the ion yield spectrum increases much faster with intensity than the fluorescence spectrum.

Experimentally, power broadening was studied in this thesis by gradually increasing the laser power and also by repeating the measurements after introducing a focusing lens that increases the intensity roughly by a factor of 45. To determine the intensity of the laser beam, the power was measured with a Thorlabs PM100D laser power meter, and its value divided by the FWHM surface of the Gaussian beam determined with the help of figures 3.11 and 3.10. The error of the power meter in the region of a couple of mW is in the order of 10%. The error of the FWHM radius of the beam is in the order of 1%. The behavior of the line shapes was experimentally determined and is presented in figures 4.7 and 4.5. Figure 4.7 presents the results for the ion spectra while figure 4.5 presents the results for fluorescence spectra under the exact same conditions. Figure 4.6 is the same as figure

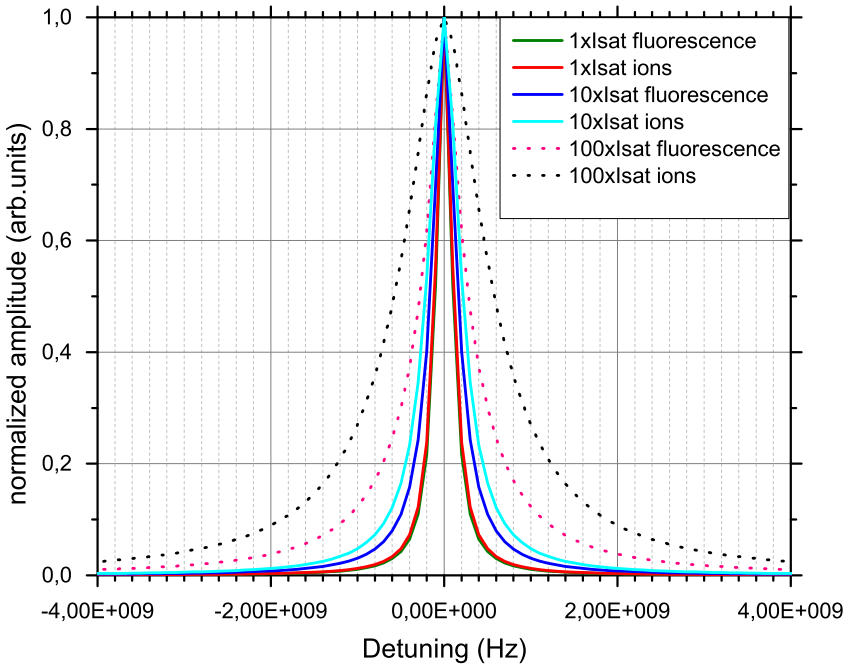

Figure 4.3: Theoretical expectation of the evolution of Lorentzian linewidths for various intensity values.

4.5 but zoomed in for the low intensity spectra.

$$N_2 = \frac{N_t}{2}\left(1 - \frac{1}{1 + I/I_{\text{sat}}}\right) \tag{4.8}$$

Of course the number of ions that are in the excited state does not only depend on the intensity of the laser beam but also on the interaction volume section of the laser beam with the atomic beam. Since the volume depends on the area of the laser beam, which is different for the measurements with the focusing lens, data have to be corrected since they address a factor of 45 less atoms. Then the data "with lens" are comparable with the data "without lens". The results are presented in figure 4.8. In this case the spectra behave rather unexpectedly. There seems to be a qualitative agreement between model and data regarding the Lorentzian width (see figure 4.4). But unlike the fluorescence spectra that showed an almost constant Gaussian width contribution independent of the intensity, the integrated

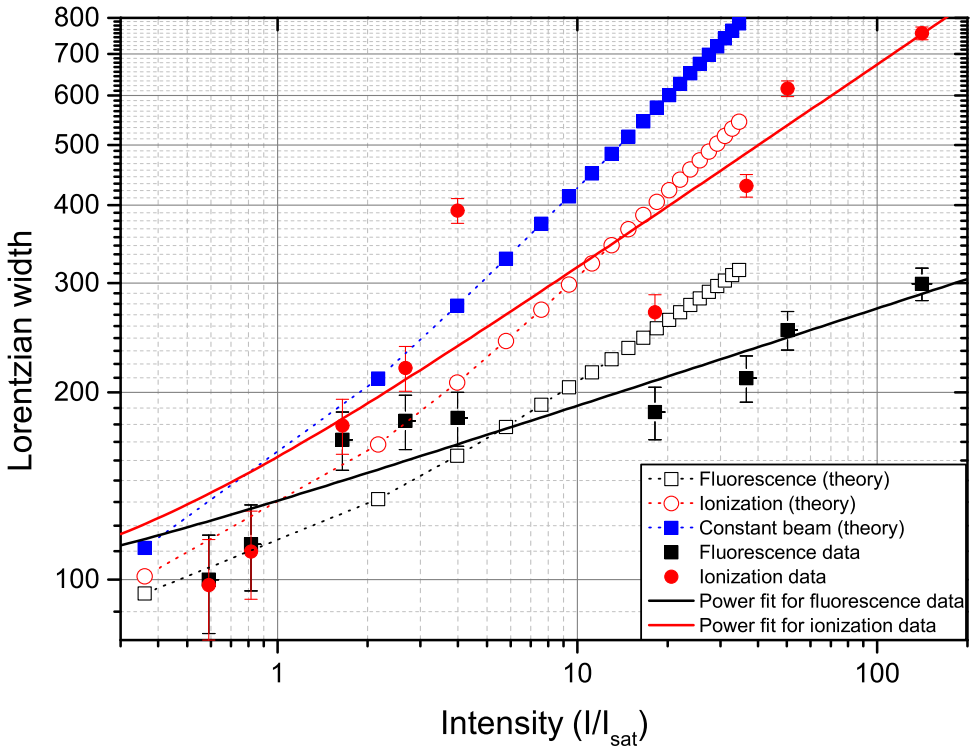

Figure 4.4: Theoretical expectations and experimental data of the evolution of Lorentzian line widths as a function of the laser beam intensity. The theoretical predictions follow power laws. The experimental data are also fitted with power laws. The function used here is $y = A(1 + \frac{x}{I_{\text{sat}}})$.

ion spectra showed an increasing Gaussian width with increasing intensity. The theoretical model described above is in this case not able to explain the Gaussian increase. However, it is a simplified model as the velocity distribution and its effects on the line shape have not been taken into account. In part, this effect is due to saturation effects on the MCP detector, but a major contribution is due to power broadening.

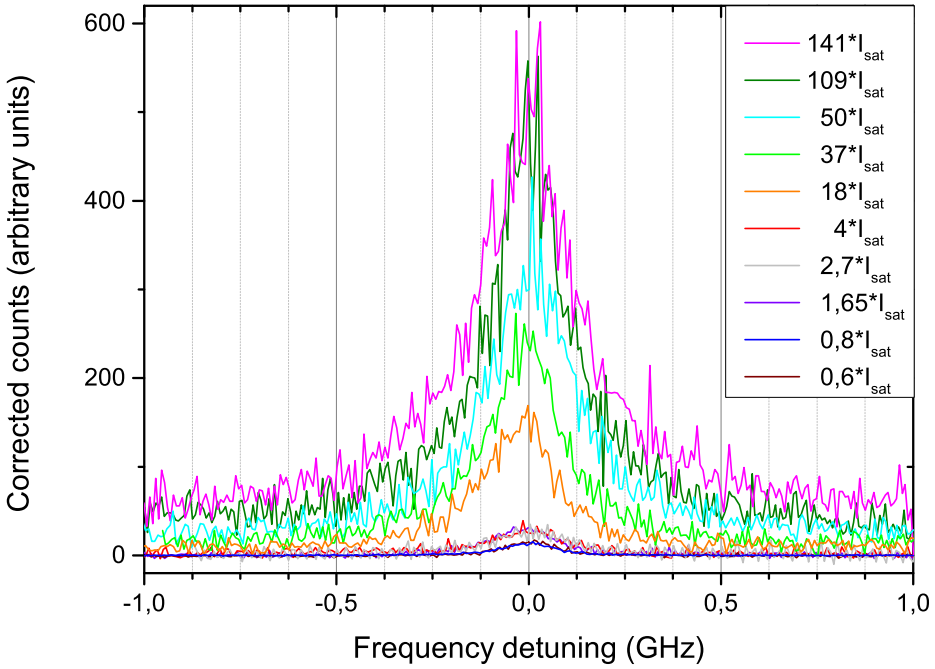

Figure 4.5: Fluorescence spectra for various intensity values expressed in units of I_{sat} with $I_{sat} = 8889\,\mathrm{W/m^2}$. The background was subtracted and the data has been smoothed and scaled by relative overlap area of laser and atomic beams.

4.3 Determination of two-photon beryllium ionization cross section

One of the aims of this thesis was the experimental determination of the two-photon ionization cross section of the Be atom with the intermediate $1s^2 2s2p\ {}^1P_1$ level. Some theoretical calculations of this cross section have been performed in the past. Moccia and Spizzo [33] calculated the cross section by employing the so called L^2 basis set. Their results were presented in a graph but unfortunately the exact cross section values are hard to read. Still the cross section at resonance can be estimated to a value between 10^{-51} and 10^{-52} m^4·s. Another publication by Smith et al. [34], presents a completely different method, namely the R-Matrix theory of two-photon absorption. However their results are in very good agreement with

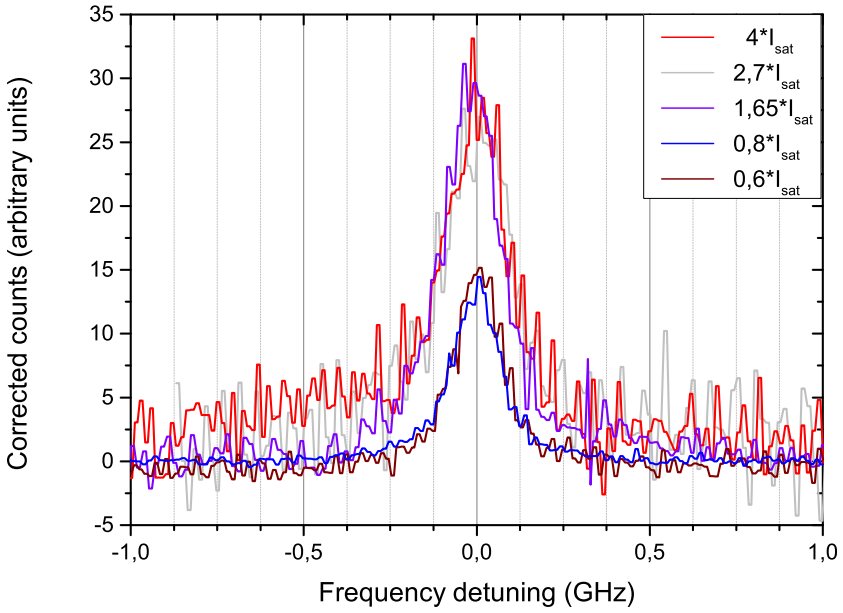

Figure 4.6: Same data as 4.5 but zoomed in for the low intensity spectra without a focusing lens. Intensity is expressed in units of I_{sat} with $I_{\text{sat}} = 8889\,\text{W/m}^2$. The background was subtracted and the data has been smoothed.

Moccia and Spizzo. Their graph allow better extrapolation of the interesting cross section, which is estimated to be $9 \cdot 10^{-52}$ m^4·s. In the next section the cross section is estimated.

4.3.1 Calculation from experiment

In the following table, the ion rate and fluorescence rate for various settings have been determined (corrected for background stray light counts).

The two-photon ionization cross section of beryllium can also be estimated with a large uncertainty calculated using our experimental data. A single photon ionization cross section is given by

$$\sigma = \frac{\dot{N}_{\text{Ion}}}{\eta \cdot V \cdot \phi} \tag{4.9}$$

where $\dot{N}_{\text{Ion}}$ is the measured ion production rate (in 1/s), η is the atomic density

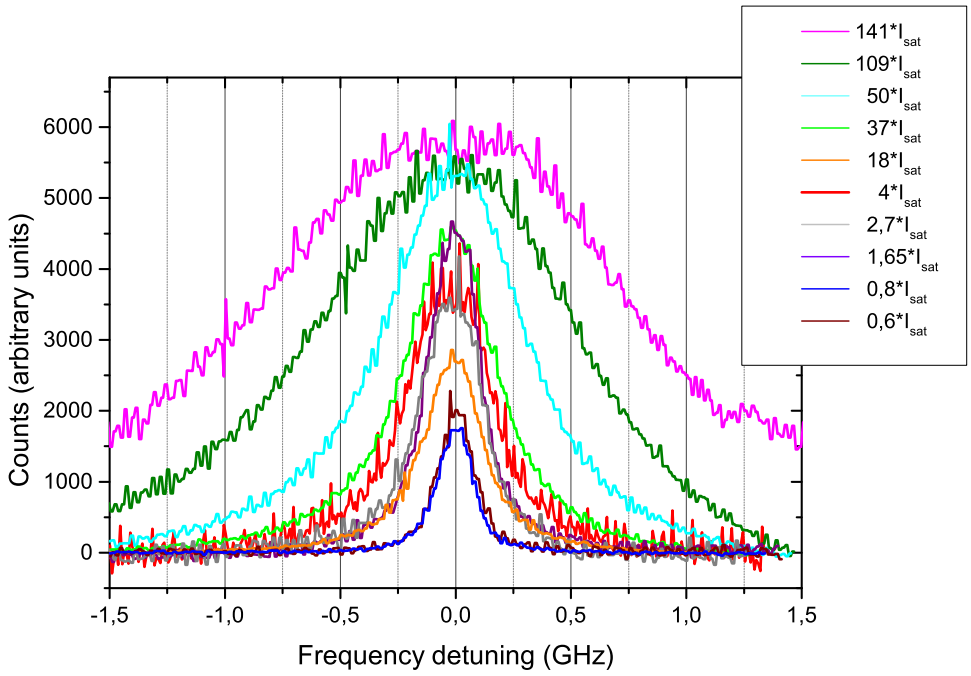

Figure 4.7: Integrated photoionization spectra, i.e., including fluorescence signal for various intensity values expressed in units of I_{sat} with $I_{\mathrm{sat}} = 8889\,\mathrm{W/m^2}$. The background was subtracted and the data has been smoothed. Please take note that five highest saturation measurements were taken with an f=500 mm focusing lens which reduces the cross sectional area with the atomic beam to a factor of about 1/45.

in the reaction region that is reduced to the number of atoms striking the quartz crystal microbalance per second per surface, divided by their most probable velocity, and ϕ is the photon flux. For a two-photon ionization process where the laser beam intensity equals the saturation intensity, about a fourth of the atoms are in the excited state, i.e. $\eta' = \eta/4$. Taking this into account, the ionization cross section of the excited atom becomes

$$\sigma = \frac{\dot{N}_{\mathrm{Ion}}}{\eta/4 \cdot V \cdot \phi.} \tag{4.10}$$

In order to determine the number of atoms in the interaction region, we use measurements performed with the quartz crystal microbalance that is installed at a distance of 100 mm from the oven. The interaction region, however, is at a distance of 75 mm from the oven so that the measured atomic density has to be corrected.

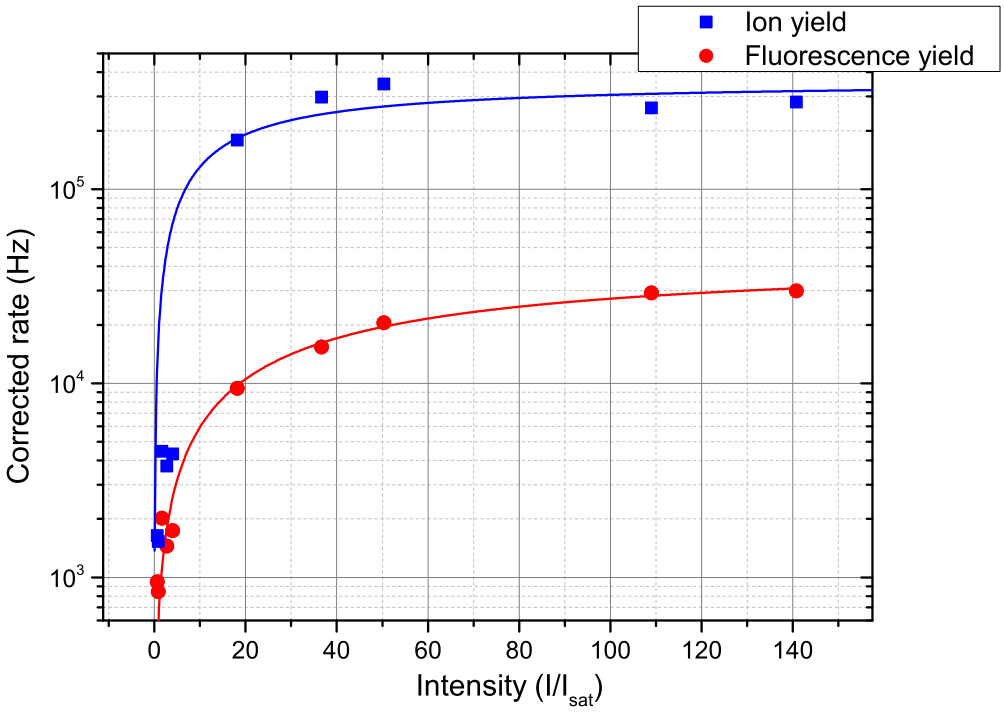

Figure 4.8: Peak ionization and fluorescence detection rates in (Hz) as a function of the laser beam intensity given in units of I_{sat} with $I_{sat} = 8889\,\mathrm{W/m^2}$. The rates measured when the focusing lens is used have been corrected since the interaction cross section with the atomic beam is smaller. The data are fitted with a function according to equation 4.8. The blue curve shows saturation of the MCP system. For the red curve, saturation is an atomic effect.

The density of the beam decreases with the square of the distance so that the density ratio can in this case be approximated by the quadratic ratio of distances. In this case the atomic density in the interaction region is about a factor 16/9. The quartz detector measures an atomic rate of about $1 \cdot 10^{12}\,\mathrm{s^{-1}}$. The area of the detector is $A_{\mathrm{quartz}} = 0.539\,\mathrm{cm^2}$ and, considering the correction factor this results in a rate per $\mathrm{m^2}$ of $3.3 \cdot 10^{16}\,\mathrm{s^{-1}m^{-2}}$. The atomic density is then easily calculated by multiplying the rate per $\mathrm{m^2}$ with the most probable velocity of the atoms (see 4.1.1) of $v = 2032\,\mathrm{m/s}$. So the total atomic density of the beam is in the order of $1.6 \cdot 10^{13}\,\mathrm{m^{-3}}$. For the determination of the ionization cross section, however, we need to know the number of atoms in the interaction region. The volume of the

	1 mm slit	**2 mm slit**	**4 mm slit**
Ion Rate without lens (Hz)	2620(262)	4560(456)	8620(862)
Fluorescence rate without lens (Hz)	1050(105)	1930(193)	1450(145)
Ion Rate with lens (Hz)	7420(742)	9340(934)	11350(1135)
Fluorescence rate with lens (Hz)	250(25)	690(69)	960(96)

Table 4.1: Rates with and without a focusing lens for different slit settings. An error of 10% is estimated due to fluctuations of the laser power.

interaction region is calculated by multiplying the area of the laser beam with the length of the region. The length of the interaction region is estimated to about 4 mm (determined from atomic beam opening angle after the 2 mm slit). The area of the beam is calculated to about 0.77 mm^2 and thus, the total interaction volume is about 3.08 mm^3 for a measurement without a focusing lens. The total number of atoms in the interaction region is then $N_{\mathrm{atoms}} = 4.9 \cdot 10^4$. In order to be able to determine the one photon ionization cross section according to equation 4.9 the photon flux is as well required, determined by

$$\phi = \frac{P}{A \cdot E_{\mathrm{ph}}}, \tag{4.11}$$

where P is the laser power, A is the laser beam area and $\mathrm{E_{ph}}$ is the energy of a single photon. At a photon flux of $1.25 \cdot 10^{22} \mathrm{s}^{-1}$ an ion rate of 4700 s^{-1} was detected. The detection efficiency of the MCP detector for ions is roughly 50%, so that we can assume the double rate of 9400 s^{-1}. Inserting all these values in equation 4.10 we get a cross section of

$$\sigma = 6 \cdot 10^{-23}\,\mathrm{m}^2 \cdot \mathrm{s} \tag{4.12}$$

for the excited atomic level of beryllium. We can improve our estimation of the factor of atoms in the excited state with the help of the fluorescence graph depicted in figure 4.8. At a fully saturated rate of about 45000 s^{-1} which can be extrapolated from the fit, a factor $1/2$ of the atoms are expected to be in the excited state. Since the fluorescence rate for our measurement is about 850 s^{-1}, the factor of excited atoms are estimated to be $f = \frac{45000}{850} \times \frac{1}{2} \approx 0.037$. With this factor, equation 4.9

results in $\sigma = 4 \cdot 10^{-22}\,\mathrm{m^2 s}$. The uncertainties for our experimental value are to high at this stage, as no model was found to explain the data accurately. Thus this value should be taken as an order of magnitude estimate. According to [35] the cross section value for this process is estimated to $\sigma = 2 \cdot 10^{-21}\,\mathrm{m^2 \cdot s}$. A simple method to calculate the direct cross section of a two photon ionization process is by using formula 4.9 modified for two photons in a weak field which corresponds to multiplying with the photon flux ϕ twice:

$$\sigma_{2\hbar\omega} = \frac{\dot{N}_{Ion}}{\eta \cdot V \cdot \phi^2}. \tag{4.13}$$

For the same values as above, this equation leads to a cross section of

$$\sigma = 4.8 \cdot 10^{-45}\,\mathrm{m^4 \cdot s}. \tag{4.14}$$

Compared to the theoretical estimations of [33] and [34], according to which σ is in the order of $10^{-51}\,\mathrm{m^4 \cdot s}$, our value is about seven orders of magnitude greater. This might mean that we are not dealing with a simple two level system as it is assumed in those models, since the coupling of the excited $^1\mathrm{P}_1$ level of Be to the continuum is strong.

5 Summary and outlook

The main aim of this thesis was to design, construct, and characterize an experimental setup that would enable the two photon ionization of beryllium atoms in order to sympathetically cool HCIs in the cryogenic Paul trap CryPTEx with the photoions that are produced. Ion and fluorescence spectral lines were measured and compared to simple models that describe the data quite well, at least qualitatively. Regarding the two-photon ionization cross sections, it should be noted that neither our simple estimates nor more sophisticated theoretical models, as in [33], reproduce the present experimental results. Most probably the assumptions underlying those calculations (e.g., weak coupling of the excited state to the continuum) are not realistic for our experimental settings. As no quantitative agreement was found, more work is needed to get to a full understanding of this unexpectedly complicated system. Nevertheless, a high rate of the photoionization of beryllium was achieved with the experimental setup constructed in the scope of this thesis. Since sufficient safety measures were taken, there is also no risk of contaminating the CryPTex main chamber with beryllium. The setup has now been mounted to CryPtex, where the first experiments with singly ionized beryllium will take place. Sympathetic laser cooling of HCI requires fast loading of Be^+ and the main prerequisite for this, the efficient photoionization of beryllium, was achieved in this thesis.

Part I

Appendix

A Oven

Figure A.1: View of all components used for the Oven.

B Electronics

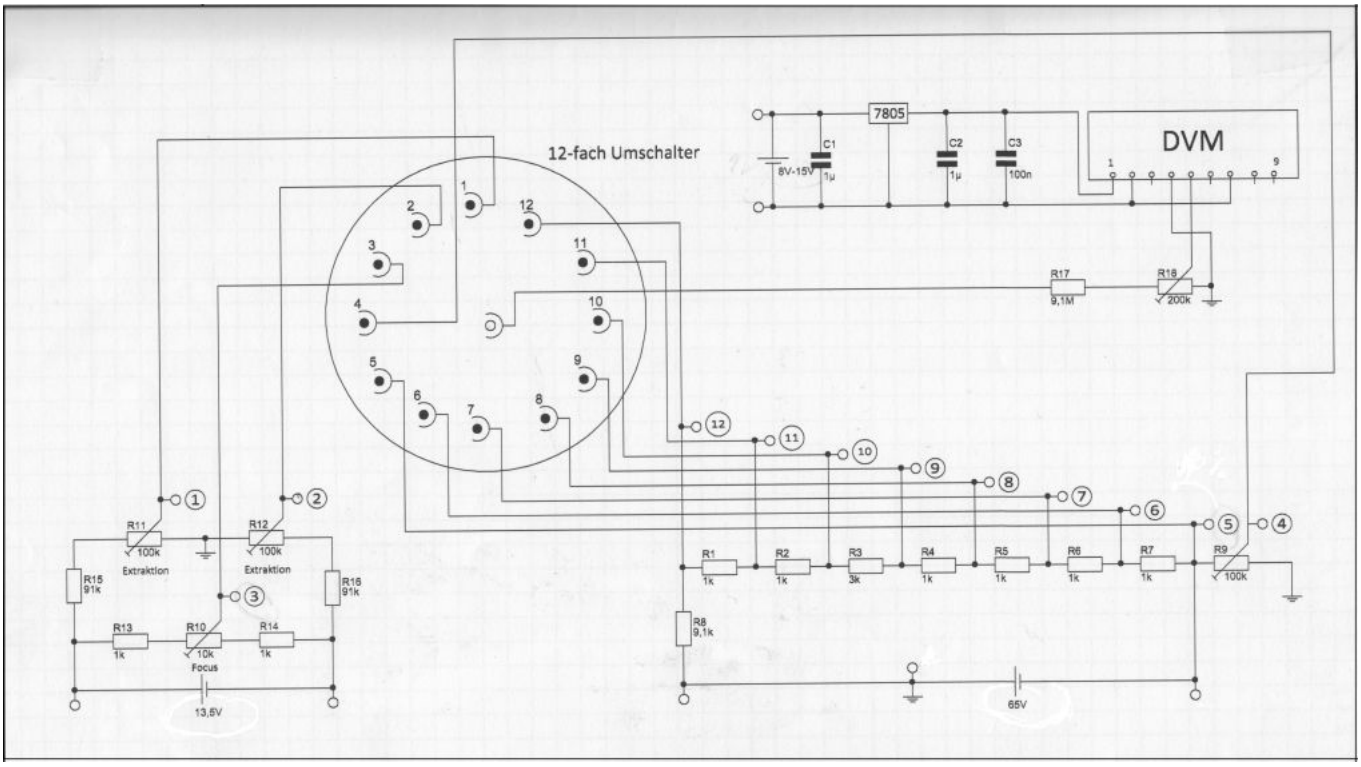

Figure B.1: Electric plan of the voltage divider used to control the electrode potentials.

C Material Safety Data Sheet of Beryllium

In the next pages a material safety data sheet of beryllium provided by Electronic Space Products International (ESPI) is attached. The information about toxicity and measurements that have to be taken when handling with beryllium are necessary for the implementation of the experiments described in this thesis. The recommended safety measurements have to be taken seriously to avoid any kind of health danger.

ELECTRONIC SPACE PRODUCTS INTERNATIONAL

1050 Benson Way, Ashland, OR 97520
Toll Free (800) 638-2581 * Fax (541) 488-8313
E-Mail: sales@espimetals.com

MATERIAL SAFETY DATA SHEET

I PRODUCT IDENTIFICATION

Trade Name: Beryllium
Formula: Be
Chemical Family: Metallic Element
CAS #: 7440-41-7

II HAZARDOUS INGREDIENTS

Hazardous Components	%	OSHA/PEL	ACGIH/TLV
Beryllium	0-100	.002 mg/m^3	.002 mg/m^3

Toxic Substances Control Act: Beryllium (CAS # 7440-41-7) is listed on the TSCA Chemical Substance Inventory of Existing Chemical Substances.
NIOSH RTECS#: DS1750000

III PHYSICAL DATA

Boiling Point: 2970 ^oC
Density (g/cc): 1.85
Atomic Weight: 9.01
% Volatiles: None
Appearance and Odor: Grey metallic, odorless
Melting Point (^oC): 1289
Vapor Pressure: N/A
Evaporation Rate: N/A
Solubility in H_2O: None

IV FIRE AND EXPLOSION HAZARDS DATA

Flash Point (Method used): Non-combustible as a solid. Ignition occurred as a powder layer consisting of 1.0 to 5.0 micron particles between 540 ^oC and 700 ^oC. Coarser beryllium powder able to pass through a 74 micron sieve did not ignite under like testing.

Explosive limits: Not applicable to solids. As a cloud of 1.0 micron diameter powder ignition occurred at 910 ^oC. Beryllium powder greater than or equal to 2 microns in diameter did not ignite under like conditions. Regardless of powder size tested beryllium did not ignite as a cloud in a spark apparatus.

Extinguishing Media: As a solid, use extinguishing media appropriate to the surrounding fire. Do not use water or carbon dioxide to extinguish beryllium powder fires. As a powder, extinguish by smothering using a Class D fire extinguisher, dry sand, graphite powder, or sodium chloride.

Special Fire Fighting Procedures: If this material becomes airborne as a respirable particulate during a fire situation, pressure-demand self-contained breathing apparatus must be worn by firefighters or any other persons potentially exposed to the metal fumes.

Unusual Fire and Explosion Hazard: Do not use water to extinguish fires around operations involving molten metal due to the potential for steam explosions. In addition, water may disassociate when in contact with burning beryllium powder or chips releasing flammable hydrogen gas which could burn and result in an explosion. Ventilation duct work which has accumulated a fine coating of

beryllium dust on its internal surface poses a potentially serious fire hazard. Extinguishing using Class D fire extinguisher media and shut down or isolate the affected portion of the ventilation system. Because of this potential risk, sources of ignition such as flame, spark, etc. must not be allowed to enter the ventilation duct work. Also, duct work must be made of non-combustible material.

V HEALTH HAZARD INFORMATION

Primary Routes of Exposure: **Inhalation**: An exposure to airborne beryllium in excess of the occupational standard can occur during routine handling, material transfer, chemical processing or further processing of powdered material and when machining, melting, casting, dross handling, picking, welding, grinding, sanding, polishing, milling, crushing, or otherwise abrading the surface of solid beryllium in a manner which generates finely divided particles. Machining operations conducted under a flood of liquid coolant usually require local exhaust ventilation. The cycling through a machine of liquid lubricant/coolant containing finely divided beryllium in suspension can result in the concentration building to a point where the particulate may become airborne during use. A filter, centrifuge, or settling chamber can be installed in-line if necessary. The potential for exposures also may occur during repair or maintenance activities on contaminated equipment such as: furnace rebuilding, maintenance or repair of air cleaning equipment, structural renovation, welding, etc.

Acute Effects:

Inhalation: This product is insoluble and does not cause acute health effects.
Ingestion: This product is insoluble and does not cause acute health effects.
Skin: Skin abrasion may cause irritation.
Eye: Injury to the eyes can result from particulate irritation or mechanical injury to the cornea or conjunctiva by dust or particulate.

Chronic Effects:

Inhalation: Overexposure to airborne beryllium particulate may cause a serious lung disease, in certain sensitive individuals, called chronic beryllium disease (chronic berylliosis). Chronic beryllium disease is a condition in which the tissues of the lungs become inflamed, restricting the exchange of oxygen between the lungs and the bloodstream. Symptoms may include cough, chest pain, shortness of breath, weight loss, weakness, and fatigue. Long term effects may include loss of lung function, fibrosis, or subsequent secondary effects on the heart with eventual permanent impairment.
Ingestion: There are no known cases of illness resulting from ingestion of beryllium.
Skin: Skin abrasion may cause irritation.
Eye: Injury to the eyes can result from particulate irritation or mechanical injury to the cornea or conjunctiva by dust or particulate.

Carcinogenic references: Hazard communication regulations of the U.S. Occupational Safety & Health Administration require that caution labels for materials listed as potential carcinogens in either the International Agency for Cancer Research Monograph Series or the National Toxicology Program Annual Report on carcinogens must contain a cancer warning. Beryllium has also been so listed based principally on animal tests and therefore this material bears a label identifying it as a potential cancer hazard.

Medical Conditions Aggravated by Exposure: Persons with impaired pulmonary function, airway diseases, or conditions such as asthma, emphysema, chronic bronchitis, etc. may incur further impairment if excessive concentrations of dust or fume are inhaled. If prior damage or disease to the neurologic (nervous), circulatory, hematologic (blood), or urinary (kidney) system has occurred, proper screening or examinations should be conducted on individuals who may be exposed to further risk where handling and use of this material may cause excessive exposure.

EMERGENCY AND FIRST AID PROCEDURES:

INHALATION: Remove to fresh air. Although no cases in which a person stopped breathing as a result of exposure are known, if breathing has stopped, perform artificial respiration and obtain medical help.
INGESTION: Swallowing metal powder or dust can be treated by having the affected person drink large quantities of water and attempting to induce vomiting if conscious. Obtain medical help.
SKIN: Remove contaminated clothing, brush material off skin, wash affected area with soap and water. If irritation persists, seek medical attention.
EYE: Flush eyes with copious amounts of clean water. If irritation persists obtain medical help. Contact lenses should not be worn when working with metal dusts and powders because the contact lens must be removed to provide adequate treatment.

VI REACTIVITY DATA

Stability: Stable

Conditions to Avoid: Oxidation will form on solid shapes when moist.
Incompatibility (Material to Avoid): Avoid contact with mineral acids and oxidizing agents which may generate hydrogen gas. Hydrogen gas can be an explosion hazard.

Hazardous Decomposition Products: Melting and dross handling or powdering operations can emit airborne dusts or fumes.
Hazardous Polymerization: Will not Occur

VII SPILL AND LEAK PROCEDURES

Steps to Be Taken in Case Material Is Released or Spilled: In solid form this material poses no health or environmental risk. If this material is in powder or dust form, establish a restricted entry zone based on the severity of the spill. Persons entering the restricted zone must wear adequate respiratory protection and protective clothing appropriate for the severity of the spill. Cleanup should be conducted with a vacuum system utilizing a high efficiency particulate air filtration system followed by wet cleaning methods. Special care must be taken when changing filters on HEPA vacuum cleaners when used to clean up potentially toxic materials. Caution should be taken to minimize airborne generation of powder or dust and avoid contamination of air and water. Depending upon the quantity of material released, fine powder or dust spills to the environment may require reporting the National Response Center at (800) 424-8802 as well as the State Emergency Response Commission and Local Emergency Planning Committee.

Waste Disposal Method: Dispose of in accordance with State, Federal and Local regulations.

VIII SPECIAL PROTECTION INFORMATION

Respiratory Protection: When potential exposures are above the occupational limits, approved respirators must be used. Exposure to unknown concentrations of fumes or dusts requires the wearing of a pressure-demand self-contained breathing apparatus. Pressure-demand airline respirators are recommended for jobs with high potential exposures such as changing bags in a baghouse air cleaning device.

Ventilation: Whenever possible the use of local exhaust ventilation or other engineering controls is the preferred method of controlling exposure to airborne dust and fume to meet established occupational exposure limits. Powders should be stored and transported in tightly sealed containers and must only be handled under controlled ventilated conditions.
Protective Gloves: Wear gloves to prevent metal cuts and skin abrasions particularly during handling.
Eye Protection: Wear safety glasses, goggles, face shield, or welders helmet.

Other Protective Equipment: No protective equipment or clothing is required when handling solid forms. Protective overgarment or work clothing should be worn by persons who may become contaminated with dusts, fumes, or powders.

Work Practices: Vacuum or wet cleaning methods are recommended for dust removal. Be certain to de-energize electrical systems as necessary before beginning wet cleaning. Vacuum cleaners with high efficiency particulate air (HEPA) filters are the recommended type. The use of compressed air to remove dusts should be avoided as such an activity can result in unnecessary short-term elevated exposures to dusts. Contaminated work clothing and overgarment should be managed in such a manner so as to prevent secondary exposure to persons such as laundry operators and to prevent contamination to personal clothing. Never use compressed air to clean work clothing.

IX SPECIAL PRECAUTIONS

Packaging and Labeling Requirements: The following requirements of the U.S. Dept. of Transportation apply only to beryllium metal powder or dust, not to solid shapes:

Shipping Name: RQ Flammable Solid, Poisonous, N.O.S. (Beryllium Metal Powder).
NOTE: **Must be marked on shipping papers and on the outside of the shipping container.**

Hazard Class:	Beryllium metal powder and dust are classified as Flammable Solid and Class B Poison. **NOTE**: **Hazard class must be included on shipping papers.**
Identification Number:	UN2926 **NOTE**: **Must be marked on shipping papers and on the outside of the shipping container.**
Label(s) Required:	Flammable Solid and Poison (For Beryllium Metal Powder or Dust Only). **NOTE**: **Place on the outside of the shipping container.**
Reportable Quantity:	10 lbs. (4.54). **NOTE**: **The RQ is limited to particles having a diameter less than 100 micrometers.**
DOT Specification Container:	Suitable for Flammable Solids. Recommended double overpack when shipping powder.
Other:	Emergency response information is provided within this MSDS. **NOTE**: **This information must be included, in some form, with the shipping papers.**

SARA Title III: Beryllium is reportable under Section 313

Issued by: S. Dierks
Date: November 1992

D Lists

D.1 List of Figures

D.2 List of Tables

E Bibliography

[1] J. K. Webb,V. V. Flambaum, C. W. Churchill, M. J. Drinkwater, J. D. Barrow. *Search for Time Variation of the Fine Structure Constant*, Phys. Rev. Lett. 82, 884–887 (1999)

[2] J. K. Webb, M. T. Murphy, V. V. Flambaum, V. A. Dzuba, J. D. Barrow, C. W. Churchill, J. X. Prochaska, A. M. Wolfe5 *Further Evidence for Cosmological Evolution of the Fine Structure Constant*, Phys. Rev. Lett. 87, 91301 (2001)

[3] J. K. Webb, J. A. King, M. T. Murphy, V. V. Flambaum, R. F. Carswell, M. B. Bainbridge.*Indications of a spatial variation of the fine structure constant*, Phys. Rev. Lett., 107, (2011)

[4] Paul Langacker, Gino Segre, Matthew J. Strassler*Implications of gauge unification for time variation of the fine structure constant.*, Physics Letters B 528, 121–128 (2002).

[5] J. D. Prestage, R. L. Tjoelker, L. Maleki *Atomic Clocks and Variations of the Fine Structure Constant*, Phys. Rev. Lett. 74, 3511–3514 (1995)

[6] T. Rosenband, D. B. Hume, P. O. Schmidt, C. W. Chou, A. Brusch, L. Lorini, W. H. Oskay, R. E. Drullinger, T. M. Fortier, J. E. Stalnaker, S. A. Diddams, W. C. Swann, N. R. Newbury, W. M. Itano, D. J. Wineland, J. C. Bergquist *Frequency Ratio of Al+ and Hg+ Single-Ion Optical Clocks; Metrology at the 17th Decimal Place*, Science 319, 1808-1812 (2008)

[7] Kramida, A., Ralchenko, Yu., Reader, J., and NIST ASD Team (2013). NIST Atomic Spectra Database (ver. 5.1), [Online]. Available: http://physics.nist.gov/asd [2013, December 10]. National Institute of Standards and Technology, Gaithersburg, MD.

[8] J. C. Berengut and V. V. Flambaum *Manifestations of a spatial variation of fundamental constants on atomic clocks, Oklo, meteorites, and cosmological phenomena*, Europhys. Lett. 97 (2012)

[9] PhD thesis by Thomas Baumann, Heidelberg 2012

[10] R. Schuman and A. B. Garrett, *The Vapor Pressure of Beryllium at 117O-134O0K.*, J. Am. Chem. Soc., Vol 66 , 442–444 (1944)

[11] PhD thesis by Maria Schwarz *Lasermanipulation von rotationsgekühlten Molekülionen in einer neuen kryogenen Paul-Falle.* Max-Planck-Institut für Kernphysik, Heidelberg 2012

[12] M. A. Levine, R. E. Marrs, J. R. Henderson, D. A. Knapp, M. B. Schneider *The Electron Beam Ion Trap: A New Instrument for Atomic Physics Measurements.*Physica Scripta, Vol. 22, 157-163 (1988)

[13] J. R. Fuhr and W. L. Wiese, *Tables of Atomic Transition Probabilities for Beryllium and Boron*, Journal of Phys and Chem Ref Data 39, 013101 (2010)

[14] W. Ketterle and N. J. Van Druten *Evaporative cooling of trapped atoms.*, Advances in atomic, molecular and optical physics, 37,:181-236, 1996

[15] Volkhard Mäckel PhD thesis*Laserspektroskopie hochgeladener Ionen an der Heidelberger Elektronenstrahl-Ionenfalle*, Max-Planck Institute for Nuclear Physics, Heidelberg.

[16] K. Schnorr, A. Senftleben, M. Kurka, A. Rudenko, J. Ullrich,C. D. Schröter, R. Moshammer et al. *Time-Resolved Measurement of Interatomic Coulombic Decay in* Ne_2, Phys. Rev. Lett. 111, 93402 (2013)

[17] J.G. Harmsen, B.J. Lewis, A. Pant and W.T. Thompson,*Beryllium brazing considerations in CANDU fuel bundle manufacture*, 11th International Conference on CANDU Fuel, Abstract

[18] L. Gruber, J. P. Holder, J. Steiger, B. R. Beck, H. E. DeWitt, J. Glassman, J. W. McDonald, D. A. Church, D. Schneider,*Evidence for Highly Charged Ion Coulomb Crystallization in Multicomponent Strongly Coupled Plasmas*, Phys. Rev. Lett. 86, 636 (2001)

[19] L. V. Keldysh *Ionization in the field of a strong electromagnetic wave*, Soviet Phys. JETP, Vol. 20, Nr. 5 (1965)

[20] H.-Y. Lo, J. Alonso, D. Kienzler, B.C. Keitch, L.E. de Clercq, V. Negnevitsky, J.P. Home *All-solid-state continuous-wave laser systems for ionization, cooling and quantum state manipulation of beryllium ions*, arXiv:1306.3780

[21] CRC Handbook of Chemistry and Physics, CRC Press, 92nd Edition, 2011.

[22] P. A. Franken, A. E. Hill, C. W. Peters, G. Weinreich, *Generation of optical harmonics*, Phys.Rev. Lett. Vol 7, No 4, Aug. 1961

[23] Georgio Tachiev and C. Froese Fischer *Breit-Pauli energy levels, lifetimes, and transition data: beryllium-like spectra* J. Phys. B: At. Mol. Opt. Phys. 32 (1999) 5805–5823

[24] D. A. Kleinman and R. C. Miller. *Dependence of second-harmonic generation on the position of the focus.* Physical Rev. 148, 302 (1966).

[25] D. A. Kleinman and G. D. Boyd *Second harmonic generation of light by focused laser beams.* Physical Rev., 145, Iss. 1, 338-379 (1966)

[26] D. A. Kleinman and G. D. Boyd *Parametric Interaction of Focused Gaussian Light Beams*, Journal of Applied Physics 39, 3597 (1968)

[27] Daniel Nigg, Diplom thesis with the title: *Aufbau eines Frequenz-vervierfachten Diodenlasers für die Photoionisation von Magnesium.*

[28] R. Schnabel and M. Kock *f-value measurement of Be I resonance line using nonlinear time-resolved laser-induced-fluorescence technique* Physical Rev. A, Vol. 61, Iss. 6(May 2000)

[29] R. C. Hilborn, *Einstein coefficients, cross sections, f values, dipole moments, and all that,*Am. J. Phys. 50, 982–986 (1982)

[30] R.E. Irving, M. Henderson, L.J. Curtis, I. Martinson, and P. Bengtsson *Accurate transition probabilities for* $2s^2\ {}^1S - 2s2p\ {}^1P$ *transition in BeI and BeII* Can. J. Phys. 77: 137–143 (1999)

[31] M. Bashkansky, P. Bucksbaum, D. Schumacher *Asymmetries in Above-Threshold Ionization.* Physical Rev. Lett. Vol. 60, No 24 (June 1988)

[32] R. W. P. Drever, J. L. Hall, F. V. Kowalski, J. Hough, G. M. Ford, A. J. Munley, H. Ward *Laser Phase and Frequency Stabilization Using an Optical Resonator*, Applied Physics B 31, 97 (1983)

[33] R. Moccia, P. Spizzo *Two-photon probabilities and photoionization cross section calculations of Be*, J.Phys. B: At. Mol. Phys. 18 (1985) 3555-3568

[34] M. T. Smith, K. T. Taylor, C. W. Clark *R-matrix theory of two-photon absorption:application to beryllium and carbon* J.Phys. B: At. Mol. Phys. 25 (1992) 3985-4004

[35] Dae-Soung Kim, Hsaio-Ling Zhou, S. T. Manson, S. S. Tayal *Photoionization of the excited $1s^2 2s2p\ ^{1,3}P_0$ states of atomic beryllium*, Phys. Rev. A 64, 042713 (2001)

[36] J. R. Fuhr and W. L. Wiese *Tables of Atomic Transition Probabilities for Beryllium and Boron* J. Phys. Chem. Ref. Data 39, 013101 (2010)

[37] W. Demtröder *Experimentalphysik 3; Atome, Moleküle und Festkörper*, Springer Verlag

[38] P. Mrowczynski, *Konstruktion und Inbetriebnahme eines Flugzeit-Spektrometers für Ionen in Ladungsaustausch-Reaktionen an der Heidelberg-EBIT*,
Diplomarbeit at Max-Planck Institut für Kernphysik Heidelberg (2010)

[39] S. Miyamoto *A theory of the rate of sublimation* Trans. Faraday Soc., 29, 794-797 (1933)

[40] Christopher J. Foot, *Atomic physics*, Oxford University Press 2005

[41] M. L. Citron, H. R. Gray, C. W. Gabel, C. R. Stroud, Jr. *Experimental study of power broadening in atwo level atom*, Phys. Rev. A, Vol.16, Nr.6 (1977)

[42] N. B. Delone, V. P. Krainov *Multiphoton processes in atoms*, Springer series on atoms and plasmas

[43] RP Photonics online encyclopedia, www.rp-photonics.com

Acknowledgements

First of all I would like to thank my supervisor José Crespo for all his support, guidance, motivation and sharing his immense knowledge with me in the past few years. His passion for physics is contagious and therefore I am thankful since he made me realize, that the fun in experimental physics is in being curious and trying to find the right answers.

I am very grateful to Oscar O. Versolato who has been the best advisor one can wish for. Without his support this work would not have been possible. Not only his knowledge, but also his eagerness to share it and his great passion for physics makes him the ideal advisor and guardian.

Special thanks to Lisa Schmöger for being a very kind and helpful laboratory partner.

I would also like to thank all my other colleagues like Sven Bernitt, Alexander Windberger, Hendrik Bekker, RenŚteinbrügge, Maria Schwarz, Ruben Schupp, Baptist Piest etc. for being a very pleasant company during the past year and being helpful and cooperative. Last but not least, I would like to thank my parents Niko and Bärbel for all their support throughout my life and studies, my sister Dione for being there for me and my boyfriend Steffen for being who he is.

Erklärung:

Ich versichere, dass ich diese Arbeit selbstständig verfasst habe und keine anderen als die angegebenen Quellen und Hilfsmittel benutzt habe.

Heidelberg, den 10.12.2013 .....